International Journal of Heat and Mass Transfer 233 (2024) 126017

Contents lists available at ScienceDirect

International Journal of Heat and Mass Transfer

journal homepage: www.elsevier.com/locate/ijhmt

Critical heat flux for flow boiling with saturated two-phase inlet in microgravity onboard the International Space Station

Issam Mudawar *, Steven J. Darges, V.S. Devahdhanush

Purdue University Boiling and Two-Phase Flow Laboratory (PU-BTPFL), School of Mechanical Engineering, Purdue University, 585 Purdue Mall, West Lafayette, IN 47907, USA

ARTICLE INFO

Keywords:
Critical heat flux
Flow boiling
Microgravity
Saturated two-phase inlet
Flow mechanism
Correlation assessment
Interfacial lift-off model

ABSTRACT

This study examines data collected as part of the "Flow Boiling and Condensation Experiment" (FBCE), which collected microgravity flow boiling data onboard the International Space Station (ISS) between February 2022 and July 2022. This study focusses on detailed analysis of critical heat flux (CHF) data for microgravity flow boiling experiments with two-phase mixture inlet, which is unavailable in the literature. n-Perfluorohexane is used in a rectangular channel with a heated length of 114.6 mm, heated width of 2.5 mm, and adiabatic height of 5.0 mm with either single- or double-sided heating. The database covers parametric ranges never before studied in long term microgravity: mass velocity of 249.8 – 1999.9 kg/m^{2}s, inlet thermodynamic equilibrium quality of 0.02 – 0.86, and inlet pressure of 120.4 – 200.4 kPa. Image sequences recorded surrounding CHF reveal the periodic passing of a relatively high concentration of liquid, termed high-density fronts, plays a key role in rewetting the wall and facilitating boiling. Trends show CHF is weakly affected by inlet pressure and mass velocity at high mass velocity, and, at low mass velocity, strongly affected by both inlet quality and mass velocity. Upon comparing the new microgravity CHF data with prior Earth-gravity vertical-upflow CHF data, the relatively weak influence of gravity on CHF during flow boiling with two-phase inlet, contrary to subcooled inlet, is established. Intricate observations of flow features suggest a wavy liquid-vapor interface with a central vapor core and boiling within the liquid sub-layer is the primary mechanism of CHF, and the *Interfacial Lift-off Model* for flow boiling CHF well predicts the present unique database evidenced by 29.2 % mean absolute error. The predictive capability of select prior correlations for flow boiling CHF is assessed for the present operating conditions, and one previously proposed by the present authors performed the best with an overall 22.4 % mean absolute error, suggesting its applicability for this unique data.

1. Introduction

1.1. Two-phase systems in future space missions

Optimizing two-phase thermal schemes can greatly reduce the size and weight of thermal management systems, which is a necessity in many aerospace applications. Specifically, a recent NASA technical report [1] emphasizes the vital role two-phase thermal management systems will play onboard future space missions. However, one challenge in designing two-phase systems for space vehicles is anticipating their performance in different gravitational environments. Aerospace applications are exposed to a wide range of gravities from hypergravity in accelerating fighter jets to microgravity in orbiting satellites. The flow regime, pressure drop, and heat transfer performance of two-phase systems may vary across these environments and deviate from that in Earth gravity (g_e). This renders design tools developed from terrestrial experiments and databases unreliable, creating a need for high-quality reduced-gravity databases [2]. When operating in a gravity-independent regime, which is achievable for both flow boiling [3] and flow condensation [4], conventional prediction methods can still be utilized. However, gravity independence may not be achievable in every two-phase system at all operating conditions.

1.2. Boiling experiments in microgravity

1.2.1. Experiments in drop towers

In order to investigate the effects of microgravity (μg_e) on boiling, numerous researchers have adopted different techniques to produce short durations of μg_e. Experiments can be performed during freefall in a

* Corresponding author.
E-mail address: mudawar@ecn.purdue.edu (I. Mudawar).

https://doi.org/10.1016/j.ijheatmasstransfer.2024.126017
Received 23 June 2023; Received in revised form 7 January 2024; Accepted 26 July 2024
Available online 1 August 2024

Nomenclature

A_c	channel cross-sectional area, [m^2]
b	ratio of wetting front length to wavelength
Bd_θ	orientation-specific Bond number, $g\cos\theta(\rho_f - \rho_g)D^2/\sigma$
Bo	Boiling number at CHF, $q''_{CHF}/(Gh_{fg})$
C	constant
c	wave speed, [m/s]
D	diameter, [m]
D_e	equivalent heated diameter, $4A_c/P_h$ [m]
D_h	hydraulic diameter, [m]
f	friction factor
Fr_θ	orientation-specific Froude number, $G^2/\left(\rho_f^2 g\sin\theta D\right)$
G	mass velocity, [kg/m^{2}s]
g	gravitational acceleration, [m/s^2]
g_e	gravitational acceleration on Earth, [m/s^2]
μg_e	microgravity, [m/s^2]
H	height of channel, [m]
h	enthalpy, [J/kg]
h_{fg}	latent heat of vaporization, [J/kg]
Δh_{sub}	h_f - h_b, [J/kg]
k	wave number, [1/m]; thermal conductivity, [W/m-K]
L	length, [m]
$\dot{m}$	mass flow rate [kg/s]
N	number of data points
P	perimeter, [m]
p	pressure, [Pa]
p_r	reduced pressure
q''	heat flux, [W/m^2]
q''_{CHF}	critical heat flux, [W/m^2]
Re_{fo}	Reynolds number, GD/μ_f
Re_k	Phase Reynolds number
T	temperature, [°C]
ΔT_{sub}	fluid subcooling, $T_{sat} - T_f$, [°C]
t	time, [s]
u	mean phase velocity, [m/s]; velocity, [m/s]
$\bar{u}_{HDF}$	mean velocity of HDF during increment triggering CHF, [m/s]
W	width of channel, [m]
We_D	Weber number based on channel diameter, $G^2D/(\rho_f\sigma)$
We_L	Weber number based on channel heated length, $G^2L_h/(\rho_f\sigma)$
x	flow quality
x_e	thermodynamic equilibrium quality
y	coordinate normal to interface, [m]
z	streamwise coordinate, [m]
z_o	streamwise location where vapor velocity just exceeds liquid velocity, [m]
z^*	streamwise location for determining vapor layer thickness and critical wavelength, [m]

Greek symbols

α	void fraction
δ	mean vapor layer thickness, [m]
ε	liquid film thickness, [m]
η	interfacial perturbation
θ	orientation angle of channel [°]
λ	wavelength, [m]
μ	dynamic viscosity, [kg/m-s]
ξ_{30}	percentage of datapoints predicted within ±30 %
ξ_{50}	percentage of datapoints predicted within ±50 %
ρ	density, [kg/m^3]
ρ''	modified density, [kg/m^3]
σ	surface tension, [N/m]
τ	shear stress, [Pa]

Subscripts

a	corresponding to heated wall 1 or 2 (= 1 or 2)
b	local bulk liquid
c	critical
co	core
d	development
D_e	calculated $D = D_e$
e	exit
exp	experimental
f	saturated liquid; bulk fluid
g	saturated vapor
h	heated
i	interfacial
in	inlet
k	either liquid (f) or vapor (g)
n	normal to heated wall
out	outlet
$pred$	predicted
s	solid
sat	saturation
sub	subcooling
tc	substrate thermocouple
w	wall
wa	heated wall (= $w1$ or $w2$)
z	local

Acronyms

BHM	Bulk Heater Module
CHF	Critical Heat Flux
CHF-	Prior to CHF
CHF+	After CHF
FBCE	Flow Boiling and Condensation Experiment
DC	Direct Current
FBM	Flow Boiling Module
FIR	Fluid Integrated Rack
ISS	International Space Station
MAE	Mean Absolute Error (%)
MST	Mission Sequence Testing
nPFH	n-Perfluorohexane
ONB	Onset of Nucleate Boiling
RMSE	Root Mean Square Error (%)
RTD	Resistance Temperature Detector
TMA	Test Module Assembly

drop tower to achieve high-quality μg_e ($g < g_e \times 10^{-4}$). Ma and Chung [5] studied flow boiling of FC-72 over a temperature-controlled platinum wire during freefall to investigate the effects of reduced gravity on heat transfer near CHF at flow velocities of 0.078, 0.22, and 0.30 m/s. As observed in their terrestrial experiments, heat transfer increased with flow velocity, but overall heat transfer was smaller in μg_e. Similarly, the value of CHF (q''_{CHF}) degraded during μg_e compared to $1g_e$ at low flow rates, but this degradation lessened as flow rate increased. They postulated that achieving a forced-convection dominance negates the influence of gravity. Similarly, bubble behavior was drastically different between μg_e and $1g_e$ at low flow rates but became more uniform as flow rate increased.

During another drop-tower experiment, Xue *et al.* [6] studied pool boiling of FC-72 at a constant subcooling of 41°C on a 1-cm^2 silicon chip.

Compared to steady boiling in $1g_e$, bubble departure frequency decreased, and bubbles grew larger in μg_e. The gravity level did not greatly impact heat transfer at low heat fluxes, and surface temperatures were consistent between μg_e and $1g_e$. At high heat fluxes, bubble departure was rapid in $1g_e$, whereas bubbles slid along the heated surface and coalesced in μg_e. The generated momentum from sliding bubbles could occasionally detach large bubbles from the heated surface in μg_e. However, heat transfer performance and CHF were degraded in μg_e due to bubbles occupying the majority of the heated surface. This experiment was expanded on by Wang *et al.* [7] with a larger 2-cm^2 silicon chip to investigate the impacts of heated surface size in subcooled μg_e pool boiling. Heat transfer trends were similar for the two chip sizes, but heat transfer performance was consistently better for the smaller chip in both $1g_e$ and μg_e. At high heat fluxes, the 1-cm^2 and 2-cm^2 chips respectively had a hemispherical bubble and an oblate vapor blanket atop them. This was attributed to the 1-cm^2 chip experiencing surface-tension-dominant boiling, also considered heater-size dependent, which is generally prevalent in small heaters and/or low gravities, and the 2-cm^2 experiencing buoyancy-dominant boiling, prevalent in large heaters and/or high gravities [8]. The differences in boiling regime attributed to q''_{CHF} for the larger chip being 20 % greater than the smaller chip in μg_e.

Drop-tower experiments of FC-72 flow boiling in a rectangular channel were performed by Liu *et al.* [9] and q''_{CHF} in μg_e was compared to different orientations in $1g_e$. During their drop-tower experiments, they recorded 5 CHF datapoints in which, q''_{CHF} was between 77.8 and 95 % q''_{CHF} of horizontal flow in $1g_e$. However, q''_{CHF} in μg_e was consistently between that for flows oriented 135° and 315° from the horizontal in $1g_e$, which the authors recommend as bounds for predicting q''_{CHF} in μg_e.

1.2.2. Experiments on sounding rockets

Another method of achieving μg_e are sounding rockets, which offer significantly longer μg_e periods than drop towers. Ohta *et al.* [10] studied pool boiling of ethanol over a transparent sapphire glass plate onboard a sounding rocket. Steady state nucleate boiling was achieved during low heat flux and high subcooling where condensation at the interface offset vapor production at the heated surface. Cases with low subcooling experienced an abrupt CHF, due to near-saturated conditions favoring vapor production. In cases with steady-state boiling, heat transfer could either be enhanced or degraded in μg_e compared to $1g_e$, depending on vapor accumulation at the heated surface.

In order to further investigate the documented effect of relatively large bubble growth in μg_e, Souza *et al.* [11] conducted pool boiling experiments of n-pentane on a downward-facing copper disc onboard a suborbital rocket. Tests were conducted with or without a 0.3 mm narrow gap between the downward-facing heated surface and the opposite adiabatic wall to vary the confinement of bubbles. Due to the adverse effects of buoyancy preventing bubble detachment from the downward-facing heater, heat transfer coefficient was higher in μg_e than $1g_e$ for the unconfined case. However, when confined, larger bubbles in μg_e resulted in ~20 % lower heat transfer coefficients than in $1g_e$.

1.2.3. Experiments on parabolic flights

Parabolic flights are a useful way to obtain μg_e data as they have relatively generous size constraints and operators can be present onboard. Oka *et al.* [12] performed subcooled pool boiling experiments of n-pentane onboard a parabolic flight. Four distinct regimes were observed in μg_e, while only three in terrestrial gravity. In both gravities, the first two regimes were a single-phase regime with no bubbles and an isolated-bubble regime, with bubble diameters less than 10 mm. In the isolated-bubble regime, bubble departure frequency was greater in $1g_e$ than μg_e. In the subsequent regime, bubbles grew to ~20 mm in diameter and coalesced at the heated wall in μg_e. These large bubbles were reduced in size by strong condensation effects away from the wall. This behavior was starkly different than in $1g_e$ where rapid detachment ensued. A unique fourth regime was observed in μg_e at high heat fluxes, where vapor slugs occupied the heated surface with some departing due to coalescence-induced inertia. The difference in bubble behavior resulted in deterioration of heat transfer coefficient up to 50 % in μg_e compared to $1g_e$.

Saito *et al.* [13] examined flow boiling of water over a horizontal heated rod in a square channel during parabolic flight. Similar to what has been observed in the aforementioned studies, bubble detachment frequency was significantly lower in μg_e, compared to on the ground. Mitigated bubble detachment resulted in the downstream section of the rod being blanketed by vapor. The discrepancy between flow patterns in μg_e and $1g_e$ was more pronounced at low flow rates, high heat fluxes, and low inlet subcoolings. Despite the drastic difference in bubble behavior in μg_e and $1g_e$, only minor differences in heat transfer performance were observed.

Narcy *et al.* [14] performed flow boiling experiments in $1g_e$ and μg_e on a parabolic flight, with HFE-7000 in a uniformly heated sapphire tube. Comparing bubble shapes and sizes for vertical upflow in $1g_e$ and μg_e, no significant differences were noticed at relatively high flow rates, but bubbles were larger and less deformed in μg_e at low flow rates. At higher heat fluxes, the flow regime transitioned to slug flow and annular flow in both gravity environments. For annular flows, the liquid film was thinner in μg_e, but the heat transfer performance remained unaffected. They observed this at mass velocities as low as 100 kg/m^{2}s. However, during subcooled boiling, heat transfer coefficients were 20 % lower in μg_e. The authors postulated this was due to lower bubble-formation frequency.

Iceri *et al.* [15] examined vertical upflow boiling of FC-72 throughout a parabolic flight and compared results during different phases of the parabola. In μg_e, larger and more circular bubbles were observed when compared to those in $1g_e$ and hypergravity. This was attributed to the dominant effect of surface tension, particularly at low flow rates. Contrary to the observations in [14], the effect of gravity was only relevant at higher qualities, $x_{e,in} > -0.1$. During annular flow, heat transfer was the lowest in μg_e. This was attributed to buoyancy in $1g_e$ and hypergravity enhancing the effects of convection by thinning the liquid layers and promoting heat transfer.

1.2.4. Experiments onboard the International Space Station

While the aforementioned methods provide valuable, cost-effective opportunities to collect μg_e data, each has its shortcomings. Drop tower experiments provide a brief μg_e period and may struggle to reach steady state [16]. Sounding rockets and parabolic flight data may contain g-jitter, caused by oscillations in the magnitude of gravity, degrading the quality of μg_e [17] and artificially enhancing heat transfer [18]. Ideally, long-duration experiments are conducted in the stable μg_e environment of outer space to validate the data collected and predictive tools developed from short-duration experiments. Previously, long-duration boiling experiments were performed on either space shuttles [19] or recoverable satellites [20,21], but more recently, the International Space Station (ISS) has been selected as an ideal environment for this task [22]. However, opportunities are limited by the large financial costs, long-term time commitments, and limited resources, such as power and physical space, onboard the ISS.

The Microheater Array Boiling Experiment (MABE) [18] consisted of pool boiling experiments onboard the ISS with n-Perfluorohexane (nPFH) on a silicon dioxide surface heated by an array of individually controlled resistance heaters. The authors parametrically studied the effects of heater size, wall superheat, subcooling, and pressure, and compared their μg_e results to previous $1g_e$ data. The authors observed ONB at lower superheats and greater degradation of heat flux with decreasing subcooling in μg_e compared to $1g_e$. In Earth gravity, boiling heat transfer was observed to be buoyancy dominated, but in microgravity, the authors observed surface-tension-dominated boiling. The authors found that during surface-tension-dominated boiling, as experienced during their ISS experiments, gravity level does not impact heat transfer. The authors used this information to update a previously

proposed scaling law [23] to predict heat transfer in any gravitational environment based on data at any different g.

The Nucleate Pool Boiling eXperiment (NPBX) [24,25] examined pool boiling of nPFH on an aluminum disc onboard the ISS. Tests examined either the dynamics of individual bubbles or the parametric trends of boiling curves. Bubble behavior in μg_e, differed from that in $1g_e$. In μg_e, bubbles slid along the heated surface and coalesced into a large bubble. At high superheats, the large bubble continually absorbed smaller bubbles, acting as a vapor sink. Overall, the effectiveness of nucleate boiling was lesser, and q''_{CHF} was drastically lower in μg_e compared to $1g_e$. The authors cautioned that heat transfer in microgravity can be strongly dependent on heater size due to the significant growth of bubbles and extrapolating results from normal to microgravity should be done with care. For example, based on the ratio of the most-dangerous Taylor wavelength to heater diameter, their heated surface could be considered an infinitely large flat plate in $1g_e$, but a small heater in μg_e.

Researchers working with the Japanese Aerospace Exploration Agency (JAXA) have outlined flow boiling experiments of nPFH in a heated tube onboard the ISS [26]. Their experiments intend to focus on heat transfer and CHF at relatively low flow rates of $G \leq 400$ kg/m^{2}s. The experiments feature nPFH flowing through heated copper and heated glass tubes, coupled with an adiabatic transparent section downstream. Detailed heat loss analysis has been performed for both single-phase [27] and two-phase inlet [28].

1.2.5. Flow boiling and condensation experiment (FBCE) onboard the International Space Station

The present work is part of the Flow Boiling and Condensation Experiment (FBCE), a collaborative project between the Purdue University Boiling and Two-Phase Laboratory (PU-BTPFL) and the NASA Glenn Research Center. FBCE is the largest and most complex fluid physics project developed for NASA research and is a team effort of national importance. Initiated in 2011, the overarching goal of FBCE is obtaining flow boiling and condensation data in μg_e onboard the ISS, integral for the success of future space missions.

FBCE was built off of years of effort at PU-BTPFL resulting in (i) development of theoretical models for fundamental two-phase flow and heat transfer mechanisms, (ii) acquisition of new databases, (iii) compilation of consolidated databases for different mechanisms and fluids, (iv) construction of *universal* heat transfer correlations applicable to multiple fluids, and (v) development of practical thermal management solutions for a broad variety of applications (computer electronics, data centers, avionics, energy, laser, microwave, radar, space, electric vehicles, materials processing, *etc.*). These efforts encompass virtually every aspect of boiling and two-phase flow including capillary flows, pool boiling, falling films, flow boiling in macro-channels, flow boiling in mini/micro-channels, jet impingement, sprays, and hybrid cooling schemes. Key takeaways regarding each configurations performance in reduced gravity applications are as follows [29].

(i) Capillary devices (*e.g.*, heat pipes, capillary pumped loops, loop heat pipes) can only tackle exceedingly small power densities.
(ii) Pool boiling (*e.g.*, using thermosyphons) in microgravity results in the formation of exceptionally large bubbles that prevent liquid replenishment of heated surfaces and culminate in unusually low critical heat flux (CHF) values. This is attributed to the lack of body force not supporting bubble detachment.
(iii) Falling-film schemes, because of reliance on gravity to drive the cooling liquid film, are inoperable in microgravity.
(iv) Jet impingement is capable of dissipating high heat fluxes, but multiple jets are required to maintain uniform surface temperatures for sensitive devices. Increasing the number of jets necessitates increasing coolant flow rate requirements, which is less desirable in space applications.
(v) Spray cooling emulates the high-heat-flux advantage of jets but achieves better cooling uniformity with a lesser flow rate by dispersing the liquid flow as fine droplets over the entire heating surface. This is one reason sprays are found in several space applications especially in fuel delivery and chill down.
(vi) Macro-channel and mini/micro-channel boiling are well suited to cooling high-heat-flux surfaces in space applications. Key to their adaptability is the ability to tackle high heat fluxes while meeting minimal size constraints (often using *cold plates*). The former is due to reliance on fluid motion (rather than body force) to flush bubbles away from heated surfaces and replenish it with fresh liquid. Channel flow boiling will be the primary focus for the present study.

The first phase of FBCE is focused on several aspects of flow boiling and deploys the Flow Boiling Module (FBM) to collect high quality heat transfer data and flow visualization, while second phase will utilize the Condensation Module for Heat Transfer (CMHT). The FBCE facility equipped with FBM, underwent a final set of ground tests in vertical upflow called Mission Sequence Testing (MST) [30,31]. Following this, the FBCE facility was launched to the ISS in August 2021, and over 200 successful experiments were completed between February 2022 and July 2022, resulting in a microgravity flow boiling database consisting of more than 10,000 heat transfer and 200 CHF datapoints. Thus far, heat transfer and flow visualization results have been reported in detail for subcooled inlet conditions with one heated wall [32] and two opposite heated walls [33] (along with the effects of heating perimeter). CHF for subcooled inlet was investigated in detail in [34], which also included assessments of the predictive capabilities of several correlations and the *Interfacial Lift-off Model* for CHF. Given the lack of experimental data for microgravity flow boiling with two-phase inlet in the heat transfer literature, the latter set of experiments with the FBM were performed to cover a wide range of two-phase inlet qualities ranging from -0.01 to 0.87 with either one or two opposite heated walls, and the experimental results and analyses of heat transfer and flow patterns are reported in [35].

1.3. Critical heat flux (CHF) for two-phase inlet

Many systems operate in the subcooled flow boiling regime where the subcooling of the liquid enhances the cooling performance. However, subcooled inlet conditions may not always be feasible in every part of a two-phase flow loop. For example, flow loops cooling a series of heat sinks or cold plates may result in two-phase inlet for the latter modules.

Kumamaru *et al.* [36] examined dryout of water with inlet qualities of 0.40 – 0.90 in a 5×5 rod bundle. Experiments were performed under high pressure, $p = 3$ – 12 MPa, and low flow rate, $G \leq 410$ kg/m^{2}s, to simulate the behavior during a loss-of-coolant-accident in the core of a nuclear reactor. Their database captured locations of dryout, indicated by a wall superheat of 20°C. Their database contained non-monotonic parametric trends of q''_{CHF} with respect to pressure, inlet quality, and mass velocity. For example, at an inlet quality of $x_{in} \approx 0.77$, inlet pressure of $p_{in} \approx 3.0$ MPa, and mass velocity of $G = 78.2$ kg/m^{2}s, dryout occurred at $q''_{CHF} = 8.71$ W/cm^2. At a significantly higher mass velocity of $G = 220$ kg/m^{2}s, the dryout heat flux decreased to $q''_{CHF} = 4.03$ W/cm^2. However, further increasing mass velocity to $G = 313$ kg/m^{2}s, resulted in a greater dryout heat flux of $q''_{CHF} = 13.8$ W/cm^2. This contradicts the conventional trend of q''_{CHF} increasing with G as observed in the studies reported in section 1.2. Upon comparing experimental results to a few correlations, the best-performing correlations were found to have assumed complete vaporization of the fluid at CHF.

Konishi *et al.* [37] studied the effects of channel orientation on CHF during flow boiling of FC-72 with two-phase inlet in a 5.0 mm×2.5 mm rectangular channel with a single heated wall. For low inlet velocities, $u \leq 0.224$ m/s, orientation had a significant influence on flow patterns

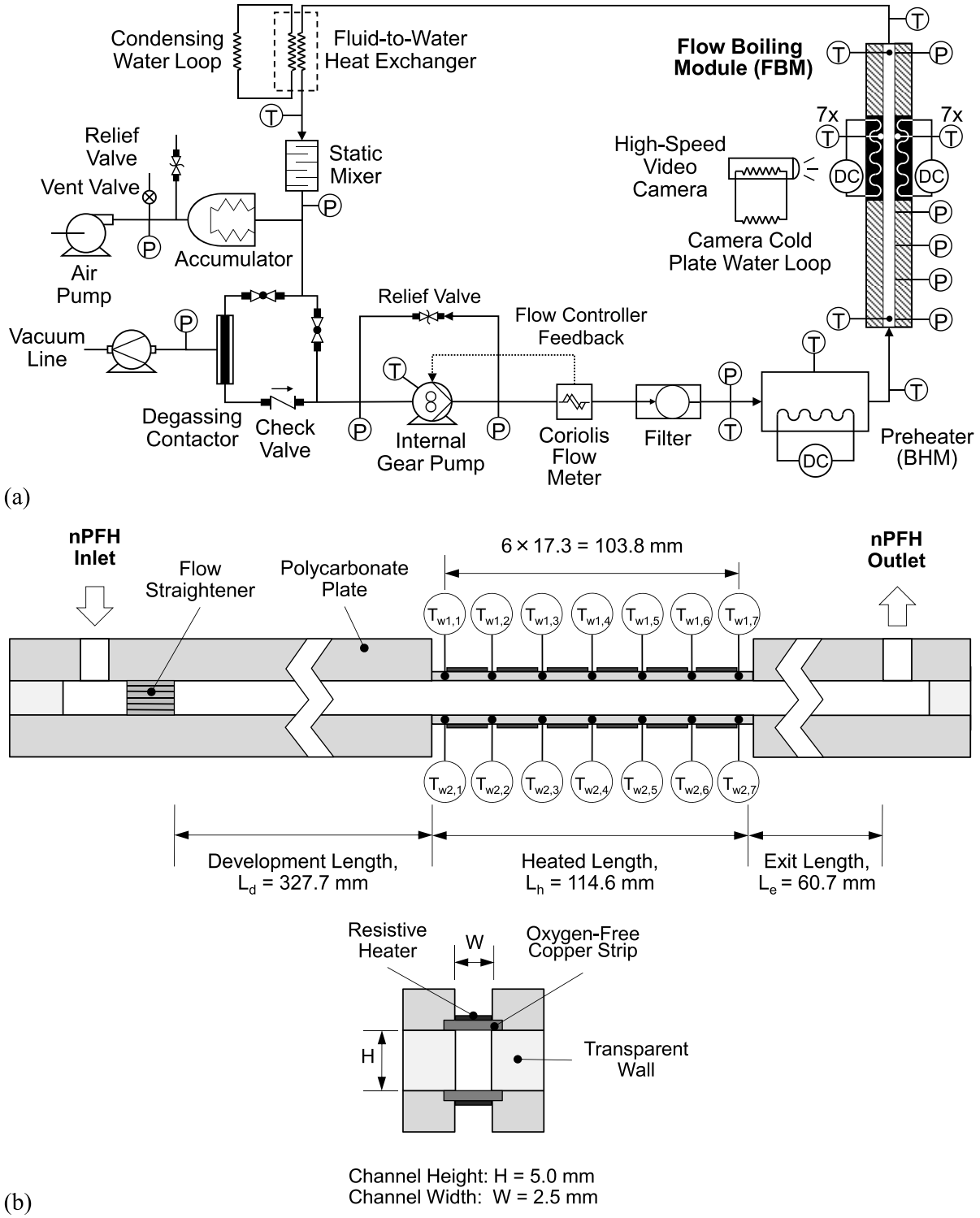

Fig. 1. Schematic diagrams of (a) the two-phase flow loop (adapted from [32]), and (b) the FBM. Designation of wall temperature measurements and key dimensions of the FBM are included.

and CHF. Near-horizontal orientations experienced stratified flow with distinct phases along the entire channel. With an upwards-facing heater, CHF occurred when significant vapor production separated the liquid layer from the heated wall. However, horizontal flow with a downward-facing heater resulted in a stratified vapor layer covering the heated wall, which resulted in significantly degraded q''_{CHF}. Vertical flows resulted in annular flow patterns throughout the entire channel. Vertical upflow experienced a higher q''_{CHF} than vertical downflow because of buoyancy aiding or impeding vapor removal from the channel, respectively. At higher velocities, $u \geq 0.398$ m/s, the differences in the observed flow patterns and corresponding q''_{CHF} at different orientations lessened. Similarly, Kharangate *et al.* [38] performed flow boiling experiments of saturated FC-72 in a rectangular channel with either one or two opposite heated walls during vertical upflow, vertical

downflow, and horizontal flow, with either the top wall, bottom wall, or both walls heated. For both single- and double-sided heating, the downward-facing heated wall limited q''_{CHF} in horizontal flow, due to the adverse effects of buoyancy. The required mass velocity to negate the effects of gravity was lesser at high inlet quality and double-sided heating, ranging from $G \approx 1230$ kg/m^{2}s for $x_{e,in} \approx 0.02$ with single-sided heating to $G \approx 410$ kg/m^{2}s for $x_{e,in} \approx 0.65$ with double-sided heating. Increasing G resulted in a monotonic increase in q''_{CHF}, but trends with respect to $x_{e,in}$ were not as clear. At low G, q''_{CHF} initially increases with increasing $x_{e,in}$, reaches a peak value, then decreases thereafter. This is explained by low inlet qualities accelerating the flow, enhancing heat transfer, prior to appreciable vapor in the channel degrading q''_{CHF}.

Tibiriçá *et al.* [39] presented CHF results of saturated flow boiling of R-134a inside a 0.38 mm horizontal tube. The authors observed a similar trend to Kharangate *et al.* [38] and q''_{CHF} initially increased with vapor quality. At an inlet quality of 0.05, q''_{CHF} increased by nearly 50 % compared to slightly subcooled conditions. The increase was attributed to the suppression of flow instabilities associated with vapor production in the test section during slightly subcooled inlet conditions. However, further increasing inlet quality degraded q''_{CHF} as less liquid was available in the incoming flow.

Dalkilic *et al.* [40] performed flow boiling experiments of R-134a in a 27-channel, 421-μm-hydraulic-diameter microchannel heat sink and studied the effects of inlet vapor quality and inlet saturation temperature on CHF. They recorded boiling curves for inlet qualities in the range of 0.01 – 0.20 at different inlet temperatures of $T_{in} = 20$, 24, and 28°C, and a constant G of 1000 kg/m^{2}s. Unlike the aforementioned studies, q''_{CHF} monotonically decreased with increasing inlet quality and decreasing saturation temperature at constant inlet quality. The authors also observed that at constant inlet quality, q''_{CHF} decreased with increasing saturation temperature due to the influence of liquid lessening as the fluid moves towards its critical point.

Gong *et al.* [41] examined the effects of heated surface orientation, mass flux, and inlet quality on flow boiling CHF. Experiments were performed with deionized water at low mass flux and low pressure, to simulate natural convection, in a 17.0 mm×10.0 mm rectangular channel. Experiments featured low inlet qualities of 0.003 – 0.036, and q''_{CHF} increased with increasing quality, agreeing with the observations at low inlet qualities in [38,39]. The authors observed conventional trends of increasing both inlet quality and mass velocity lessening the influence of orientation.

Luo *et al.* [42] used a turntable to simulate hypergravity in flow boiling experiments of R-245a in a horizontal copper tube of 2.43 mm inner diameter. They tested inlet vapor qualities of 0.10 – 0.67 in gravities between $1g_e$ and $2.77g_e$. The authors observed q''_{CHF} decreasing with increasing x_{in}, but to a lesser extent at low qualities near saturation. At a low mass velocity of $G = 156.7$ kg/m^{2}s, q''_{CHF} was significantly enhanced in hyper gravity. Also, q''_{CHF} increased almost linearly with decreasing vapor quality, even near saturation. However, at a higher mass velocity, q''_{CHF} was nearly identical at different gravity levels for a fixed x_{in}.

Clearly, a small portion of CHF literature is focused on flow boiling with two-phase inlet, and no such study is available for microgravity conditions. The present study addresses this lack of experimental data and information, crucial for the development of future space missions.

1.4. Objectives of present study

As highlighted above, this study is part of a series of studies culminating from the FBCE, a large-scale effort to obtain crucial two-phase heat transfer data onboard the ISS. The present work focuses on the CHF results obtained during flow boiling experiments in long duration μg_e with two-phase inlet, the first of its kind, presented in [35]. Flow visualization results are analyzed to investigate the complex flow patterns near CHF, conclusions from which are then used to explain the parametric trends of CHF in μg_e with respect to mass velocity, inlet thermodynamic equilibrium quality, inlet pressure, and heating configuration. Parametric trends of dimensionless groups related to the CHF mechanism are examined. The newly acquired CHF data in μg_e are compared to CHF data for vertical upflow in $1g_e$. Observations of flow patterns and mechanisms surrounding CHF justify the applicability of the *Interfacial Lift-off Model*, which is then used to confirm its ability of predicting q''_{CHF} for the present experiments. Finally, select correlations from the literature, which have previously been used to good effect to predict q''_{CHF} for two-phase inlet flow boiling experiments in Earth gravity, are assessed for their predictive capability for this unique microgravity database.

2. Experimental methods

Only a brief overview of the experimental methods is presented in this section. Comprehensive details regarding the flow loop, its implementation on the ISS, test module construction, instrumentation, measurement uncertainties, operating procedure, and data reduction are provided in [32].

2.1. Two-phase flow loop

Liquid n-Perfluorohexane (nPFH), chosen for its potential in aerospace applications [43], is pumped through a two-phase flow loop, shown in Fig. 1(a), by a gear pump. Connected in parallel across the pump are two bypass relief valves set to crack open if the pressure difference across the pump exceeds 199.5 and 206.8 kPa. Subcooled fluid passes through a Coriolis flow meter, which measures the flow rate and provides feedback to the pump, and a filter prior to entering the preheater, called the Bulk Heater Module (BHM). In the present study, a precalculated amount of heat is supplied by the BHM heaters to vaporize a portion of the liquid and establish the desired two-phase inlet conditions. The two-phase mixture passes through the FBM, absorbing additional heat, before rejecting heat in a fluid-to-water heat exchanger, returning the fluid to a subcooled liquid.

Additional components include an air-filled accumulator comprised of stainless-steel bellows connected at a T-junction downstream of the static mixer. The accumulator acts as a reference point for system pressure and dampens flow loop instabilities, and its air-side pressure is controlled by an air pump and vent valve. A pressure relief valve on the air side is set to crack open if the pressure differential between the two sides exceeds 137.9 kPa. Between the accumulator T-junction and the pump, are two parallel paths, one used during normal operation and provides direct access to the pump, while the other containing the degassing contactor is only used during degassing. The nPFH was routinely degassed to remove non-condensable gases and ensure reliable data was obtained.

2.2. Flow boiling module

The FBM consists of three transparent polycarbonate plates clamped between two aluminum support plates to mitigate leaking and buckling. The flow channel is formed by milling a 5.0 mm high and 2.5 mm wide slot into the middle polycarbonate plate. As depicted in Fig. 1(b), the FBM features a 327.7 mm developing length with a honeycomb flow straightener, a 114.6 mm heated length, and a 60.7 mm exit length. The heated walls are constructed from 114.6 mm long, 15.5 mm wide, and 1.04 mm thick oxygen-free copper strips, each having a set of six thick-film resistive heaters soldered to its back, opposite the flow channel. The heaters are electrically connected in parallel, and each has a resistance of 188-Ω. Substrate thermocouples are placed directly into the heated strips between each successive resistive heater, and the resulting small gaps between heaters do not impact the heat flux distribution along the copper strips given the high thermal conductivity of copper. This heated wall design has previously shown the ability to provide fast temperature

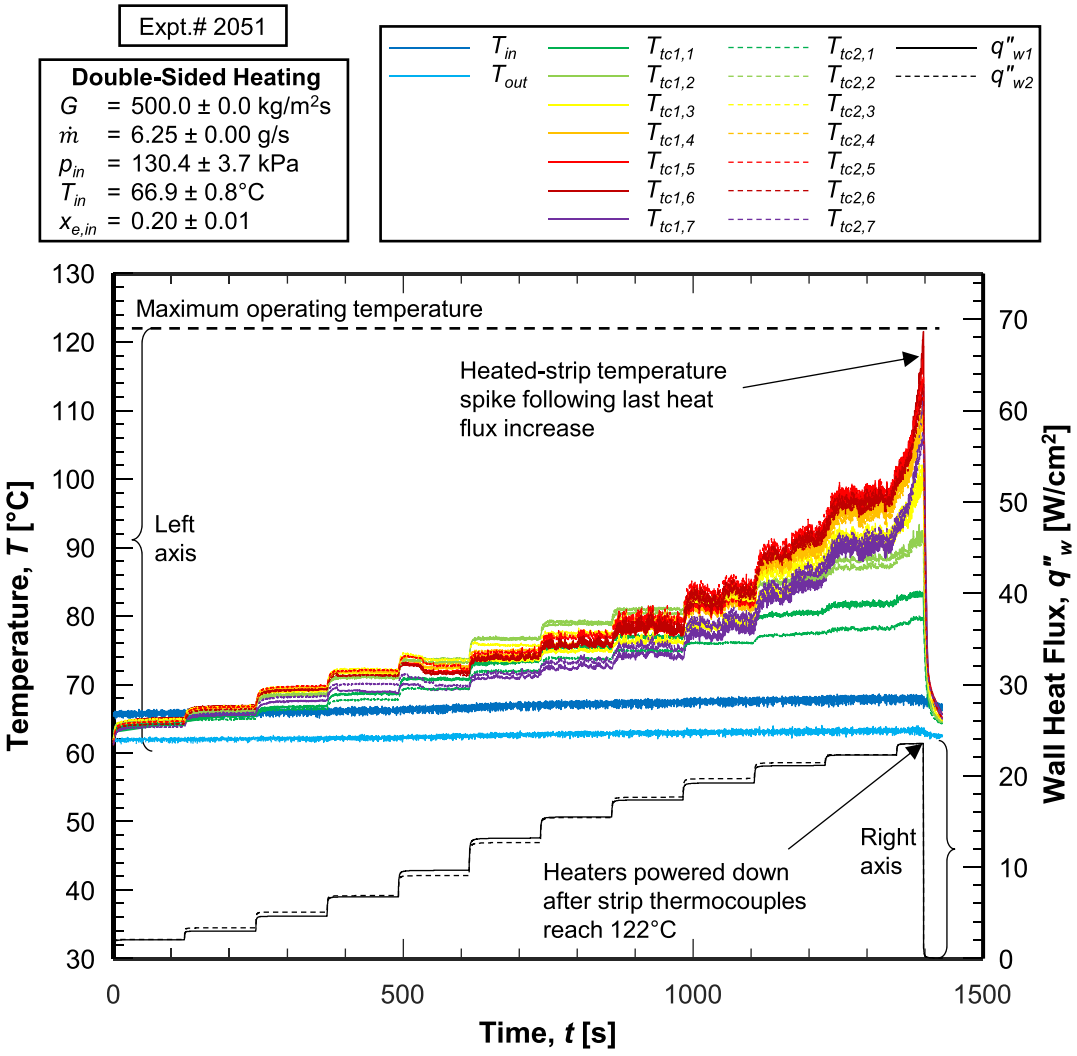

Fig. 2. Temporal variations of fluid inlet, fluid outlet, and heating-strip temperatures for heat flux increments from a minimum until CHF for a typical double-side-heated experimental case. The operating conditions are a mass velocity of 500 kg/m^{2}s, mass flow rate of 6.25 g/s, inlet pressure of 130.4 kPa, inlet temperature of 66.9°C, and inlet quality of 0.20.

response and accurate CHF measurement [44].

The transparent polycarbonate plates allow for visual access to the FBM's heated section. The polycarbonate was vapor polished to minimize vignetting effects caused by the copper strips and O-rings (used for sealing). A high-speed video camera, fitted with a F#0.95-2.5 mm lens, captures images with a resolution of 2040×164 pixels at 2000 frames per second and a shutter speed of 10 μs. The polycarbonate wall opposite the camera is backlit with blue light emitting diodes (LEDs) through a light-shaping diffuser.

2.3. Instrumentation and measurement uncertainty

Absolute-pressure-transducer measurements immediately upstream and downstream of the FBM's heated length are respectively reported as the inlet pressure, p_{in}, and the outlet pressure, p_{out}, in this study. Type-E thermocouples inserted directly into the fluid near the FBM's inlet and outlet respectively measure the fluid's inlet temperature, T_{in}, and outlet temperature, T_{out}. Additionally, type-E thermocouples inserted into the copper strip measure the heated-strip temperature. Pressures and temperatures at other locations in the flow loop are measured by pressure transducers and thermocouples and RTDs, respectively.

The FBCE flight software monitors and controls two DAQs and all other instruments. One of the DAQs collects thermocouple measurements while the other measures the output from various other sensors, including the current and voltage supplied to both the FBM's heated strips and the BHM to calculate power. The maximum measurement uncertainty in absolute pressure is ± 0.7 kPa, temperature (using thermocouples) is ± 0.5°C, temperature (using RTDs) is ± 0.5°C, FBM heater power is ± 0.3 %, BHM heater power is ± 0.6 %, and flow rate is ± 0.6 %.

2.4. Operating procedure and data processing

The desired inlet conditions (flow rate, pressure, and quality) are remotely set, and the system is allowed to become steady. FBM heating begins once steady state conditions are detected and DC power is supplied to either one or both sets of FBM heaters for single- and double-sided heating, respectively. Single- and double-sided heating are selected to (i) understand the undisturbed evolution of both the bubble boundary layer and the vapor layer on the heated wall, (ii) understand the effects of interactions between vapor layers produced on the two opposite walls, and (iii) to enable good quality flow visualization of the heated section of the test module, which is more prevalent for subcooled inlet conditions. At each heat increment, the software waits for 120 – 180 s to obtain steady-state data before increasing the FBM's heater set point to the next increment. The final 20 s of data for each heating

Table 1
Summary of CHF datapoints obtained with saturated inlet conditions to the FBM's heated section.

	Single-Sided Heating	Double-Sided Heating
Mass velocity, G [kg/m^{2}s]	249.8 – 1600.0	249.8 – 1999.9
Mass flow rate, $\dot{m}$ [g/s]	2.25 – 20.0	2.25 – 25.0
Inlet pressure, p_{in} [kPa]	120.4 – 173.9	124.5 – 200.4
Inlet temperature, T_{in} [°C]	66.5 – 77.8	66.9 – 80.7
Inlet quality, $x_{e,in}$	0.06 – 0.86	0.02 – 0.86
Outlet pressure, p_{out} [kPa]	112.9 – 158.2	115.0 – 181.2
Outlet temperature, T_{out} [°C]	59.0 – 70.3	59.3 – 79.1
Outlet quality, $x_{e,out}$	0.16 – 0.94	0.14 – 0.97
Critical heat flux, q''_{CHF} [W/cm^2]	7.9 – 28.6	6.1 – 27.8
Number of data points, N	30	45

increment are averaged to obtain steady values. The first twelve heater set points are preselected based on an estimated q''_{CHF}, after which, the set point is increased by 1.25 W to accurately capture q''_{CHF}. This continues until CHF is detected by one of the FBM heated-strip temperatures reaching 122°C.

Temporal records of temperatures and wall heat flux for a typical run are presented in Fig. 2. Notable features include: (i) inlet fluid temperature is consistently higher than the outlet due to saturation conditions within the FBM, (ii) heated-strip temperatures consistently increase with each heat flux increment, (iii) steady state is attained for almost all heat fluxes, although this is not clear at large heat fluxes due to the two-phase-mixture instabilities (discussed in section 3) causing small temperature fluctuations, (iv) the spiking trend of heated-strip temperatures to 122°C right after the last heat flux increment is set confirms this is in fact a result of CHF occurrence, and (v) heaters are powered down after strip temperatures reach 122°C. At the end of each heating increment, the final 1.0-s of recorded video is saved, but upon CHF being detected, the final 7.0-s of recorded video is saved to better capture the mechanisms causing CHF.

The FBM's inlet enthalpy is determined via energy balance over the BHM as

$$h_{in} = h_{BHM,in} + \frac{q_{BHM}}{\dot{m}}. \tag{1}$$

Fluid enters the BHM as a subcooled liquid, so the enthalpy, $h_{BHM,in}$, is determined at local temperature and pressure. The heat input to the BHM, q_{BHM}, is adjusted for heat loss between the BHM and FBM as detailed in [35]. Thermophysical properties of nPFH are evaluated using NIST-REFPROP [45]. The FBM's outlet enthalpy is determined by energy balance as

$$h_{out} = h_{in} + \frac{q''_w P_h L_h}{\dot{m}}, \tag{2}$$

where q''_w is wall heat flux, $\dot{m}$ mass flow rate, and L_h heated length. P_h corresponds to the heated perimeter of the channel and is equal to the channel width, W, for single-sided heating and $2W$ for double-sided. Prior studies have estimated the FBM's heat loss is negligible compared to the power supplied [32], so q''_w is simply calculated as the FBM heater power divided by the heated area. Thermodynamic equilibrium quality is determined as

$$x_e = \frac{h - h_f|_p}{h_{fg}|_p}, \tag{3}$$

where the inlet and outlet values are determined by setting $h = h_{in}$ and $h = h_{out}$, respectively.

The reported q''_{CHF} is the average of the q''_w causing the heated-strip temperatures to reach 122°C and the q''_w of the previous steady increment. The true q''_{CHF} will exist between the two, producing a q''_{CHF} isolation error. Considering both the heater-power measurement uncertainty and the isolation error, the maximum uncertainty in q''_{CHF} is 6.8 %, while the average uncertainty is 2.3 %. Other reported parameters corresponding to CHF, such as pressure, temperature, flow rate, *etc.*, belong to the previous steady step; this is done to avoid averaging the unsteady values during the CHF transient. A summary of CHF datapoints obtained with saturated inlet conditions to the FBM's heated section is reported in Table 1.

3. Flow visualization results and discussion

This section is focused on flow patterns observed within the FBM's heated length near CHF. Images are presented for both single-sided and double-sided heating. For single-sided heating, the selected wall impacts neither flow patterns nor heat transfer performance [32]. In each image, fluid enters the channel from the bottom and flows upwards, and heat is supplied by either the left wall or right wall, or both walls in single-side and double-sided heating, respectively.

Image sequences are presented for two conditions: a heat increment preceding CHF with $q''_w > 90\,\% \; q''_{CHF}$ (designated as "CHF-") and just after CHF occurs (designated as "CHF+"). As discussed in [35], two-phase inlet produces periodic flow patterns within the FBM. Flow patterns within the FBM over an extended period, with 25 ms interval between images, during CHF- are presented in Fig. 3(a). From 0 to 500 ms, the channel is mostly occupied by a high-quality vapor-abundant mixture, called a low-density front (LDF), and appears light. However, low-quality, liquid-abundant waves, called high density fronts (HDFs), which appear darker due to the complexities of numerous interfacial features, propagate through the channel. At 525 ms, a long HDF enters the channel, and a period dominated by HDFs persists until 750 ms. After this HDF-dominant period, another LDF-dominant period starts, and the cycle continues.

Figs. 3(b) and (c) show image sequences during the LDF- and HDF-dominant period, respectively, with a finer temporal spacing of 2 ms. During the LDF-dominant period in Fig. 3(b), a short HDF traverses the channel and gradually fades as boiling occurs within. During the HDF-dominant period in Fig. 3(c), a dark patch of liquid enters the channel. As it travels downstream, boiling is prevalent along the heated wall, trailing the HDF. Within this period, liquid presence within the LDFs is also greater, evident by the darker and textured appearance.

All selected images in the subsequent figures represent the average flow pattern within the channel, between the two extremes. However, during CHF-, only one second of video is recorded and an entire cycle of flow patterns is not always captured. In these cases, images at CHF+ are selected to best match those at CHF- to capture the flow pattern differences prior to CHF and at CHF. Accompanying each set of images are the corresponding operating conditions at CHF, as described in section 2.4. A broad range of operating conditions are presented to examine the effects of mass velocity, inlet quality, inlet pressure, and heating configuration on flow patterns around CHF in μg_e. Takeaways from this section include both parametric trends and physical mechanisms of CHF.

3.1. Interfacial characteristics near CHF

CHF is presumed to occur when vapor production within the liquid film, which appears to be replenished by the passing of HDFs, limits liquid contact with the heated wall. Fig. 4 depicts a sequence of enlarged images of the upstream quarter of the channel length as flow enters with a fleeting flow pattern of distinct features. An annular vapor core encased in a liquid film enters the channel, and boiling begins at the upstream edge of the channel within the liquid layer. The vapor layers rapidly grow along the wall, lifting the liquid layer off the wall, while also trying to reach the central core of the channel due to the tendency of faster-moving vapor to occupy the low shear region and slower-moving liquid left to occupy the high shear region. This results in a turbulent liquid-vapor mixture propagating through the channel further downstream. Typical flow patterns entering the channel are more complex, but analogous phenomena are observed. The other phenomenon noticed

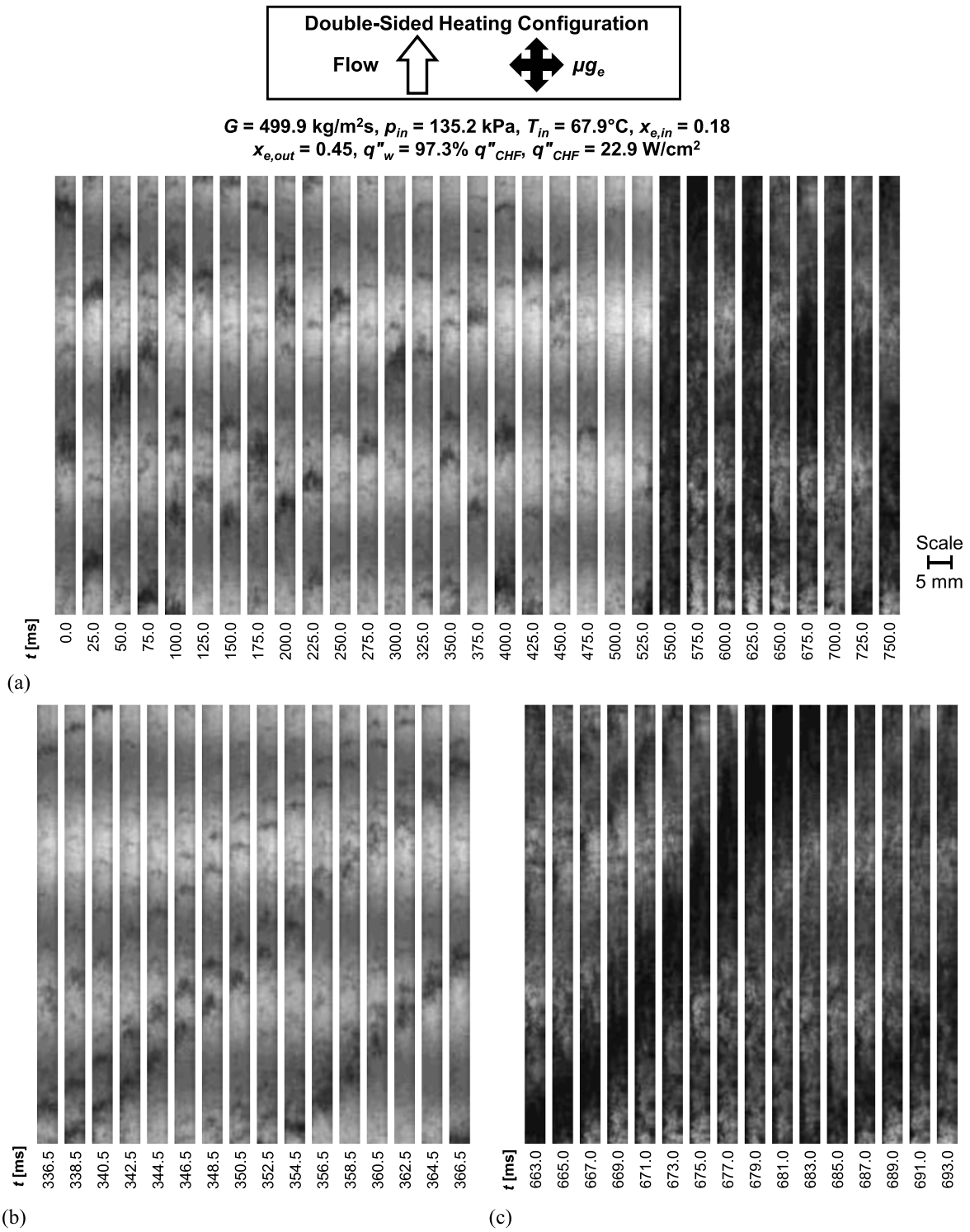

Fig. 3. Flow visualization image sequences for double-sided heating with a mass velocity of $G = 499.9$ kg/m^{2}s, inlet quality of $x_{e,in} = 0.18$, and wall heat flux of $q''_w = 97.3\,\%\ q''_{CHF}$. Shown are (a) the overall transient behavior over an extended time period (25 ms between images), (b) low-density-dominant period (2 ms between images), and (c) high-density-dominant period (2 ms between images). Channel width is 5 mm.

is, as time passes, how boiling within the liquid layer near the channel inlet thickens the vapor layer underneath the liquid layer resulting in a wavy interface.

Fig. 5 presents an image sequence at CHF during a different case displaying typical flow patterns. Images are enlarged into the upstream quarter of the channel length to highlight the interfacial behavior causing CHF. Below each image is the corresponding phase contour to accentuate the liquid layer and vapor near the heated wall. At the beginning of the sequence, a relatively dark liquid layer is observed at the upstream edge of the left, heated wall, trailing a passing HDF. As time progresses, the HDF propagates through the channel, a predominantly vapor LDF enters the channel, and the residual liquid layer slides along the wall downstream. Within the liquid layer remaining on the left wall, lighter regions initiate near the wall, expand away from the wall towards the channel core as boiling occurs, and lift the darker, more pronounced interface away from the wall. At CHF, the liquid layer

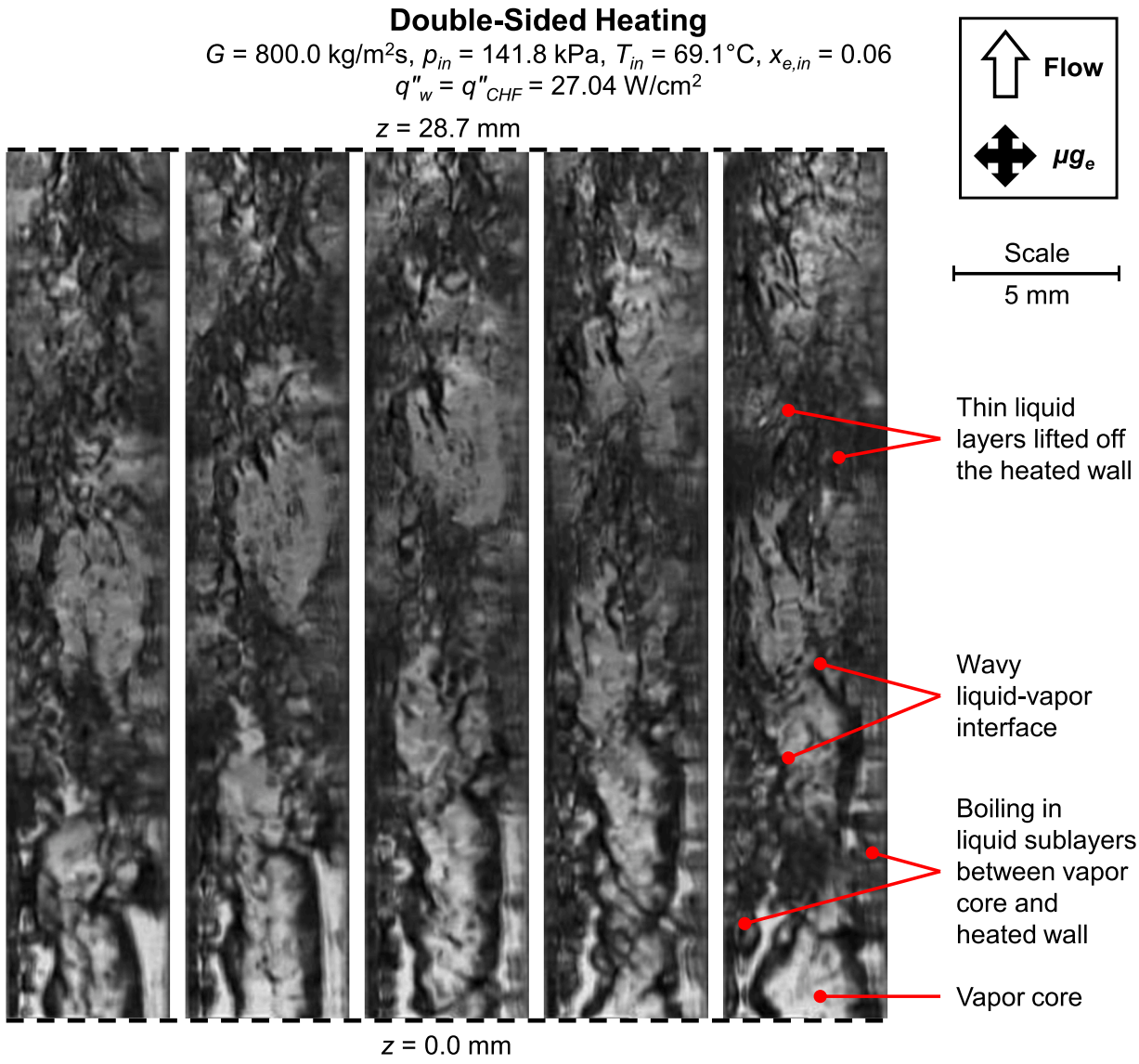

Fig. 4. Flow features in the channel's upstream region at CHF for double-sided heating with a mass velocity of $G = 800.0$ kg/m^{2}s and inlet quality of $x_{e,in} = 0.06$. A distinct annular flow enters the channel. Time interval between successive images is 1 ms. Channel width is 5 mm. Notice how boiling evolves along the flow direction and with time.

deposited along the heated wall by a passing HDF provides insufficient cooling and is quickly evaporated. By the end of the sequence, the considerably dark liquid film initially present at the upstream edge exits the frame as a swath of liquid unattached to the wall, and a lighter vapor buffer shields the wall from any remaining liquid.

Subsequent image sequences focus on the traversal of HDFs and LDFs through the channel, and their influence on the liquid film along the heated walls leading up to and at CHF. The detailed intricate observations in the present subsection cement the mechanism behind CHF for flow boiling with two-phase inlet and pave the way for applicability of the *Interfacial Lift-off Model*, which is further discussed in section 5.1.

3.2. Images at constant mass velocity

3.2.1. Effects of inlet quality for single-sided heating

Fig. 6 contains images for single-sided heating with a constant $G \approx 500.0$ kg/m^{2}s but $x_{e,in}$ varied in the range of 0.15 – 0.50. Fig. 6(a) features the lowest inlet quality of $x_{e,in} = 0.15$ and liquid ripples are observed throughout the channel, even within the LDFs. At CHF-, as the HDFs pass, a thin layer of liquid is observed along the heated left wall, accentuated by red arrowheads for demonstration. The liquid film exists trailing the downstream HDF as it exits the channel. This is interpreted as the primary mechanism in rewetting the wall and facilitates boiling within the liquid sublayer, as shown in Fig. 5. At CHF+, a HDF enters the channel in the first image and a thin liquid layer is observed along the left, heated wall. The liquid layer thins and lightens as the HDF travels downstream. By the final image in the sequence, the liquid layer is mostly depleted and only a few remnants are visible along the heated wall as the HDF reaches midway along the channel. At this point, the remaining liquid contacting the heated wall is insufficient to prevent CHF from occurring.

Images of slightly higher inlet quality, $x_{e,in} = 0.22$, are shown in Fig. 6(b), albeit, during a period that contains more vapor than that deemed average. Nonetheless, at CHF-, a HDF enters the channel and rewets the heated wall upstream. At CHF+, a HDF enters the channel and rewets the wall near the inlet. Similar to CHF -, at CHF+, boiling occurs within the trailing liquid layer as the HDF propagates downstream. However, the residual liquid is quickly depleted, and the wall becomes dry in a shorter distance from the inlet than at CHF-. At this point, liquid is only able to contact the heated wall within the HDF and

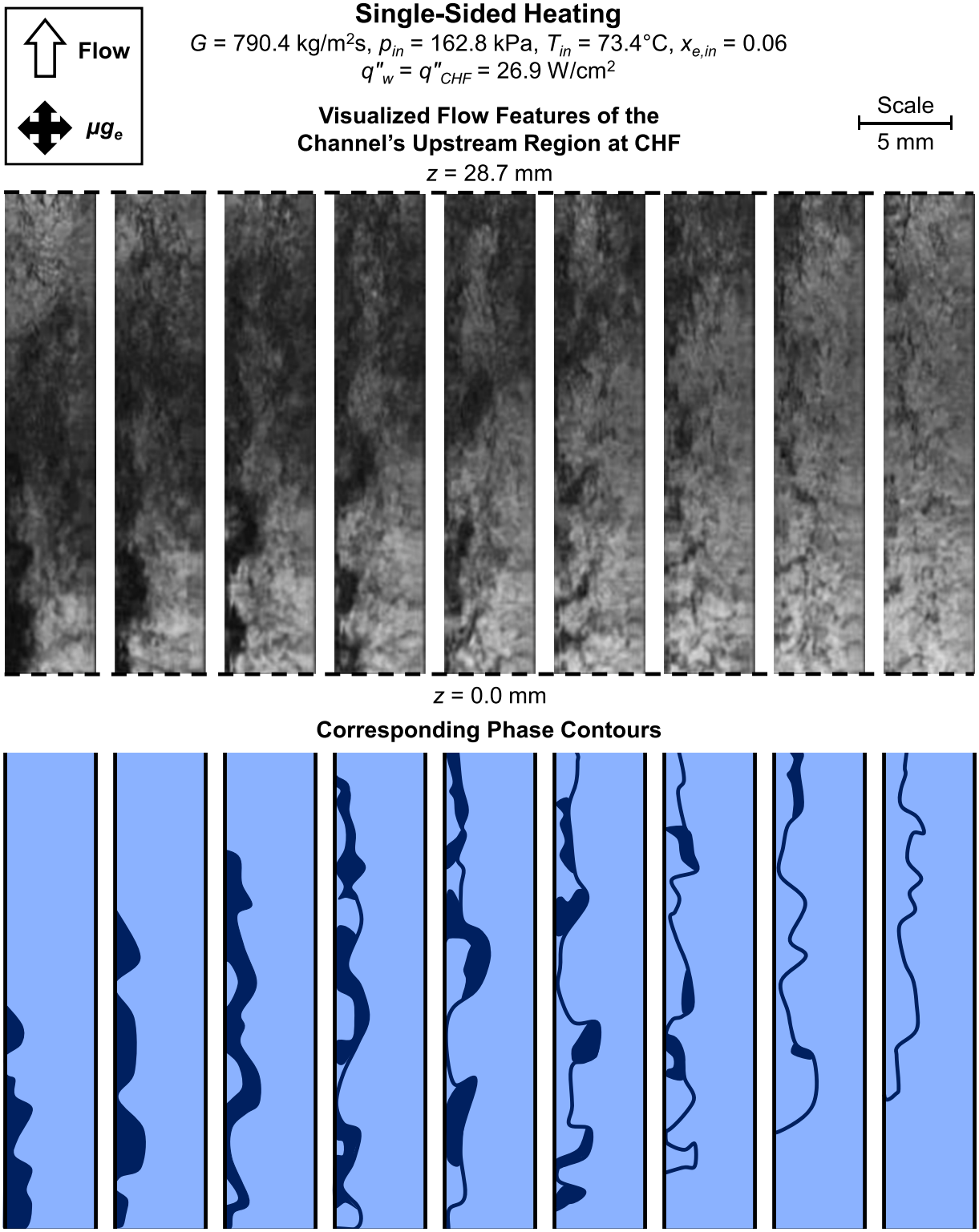

Fig. 5. Flow features of the channel's upstream region at CHF for single-sided heating with a mass velocity of $G = 790.4$ kg/m^{2}s and inlet quality of $x_{e,in} = 0.06$. The corresponding visualized phase contours are included below. Successive images are 1 ms apart. Channel width is 5 mm.

the remaining portion of the wall is completely dry, triggering CHF.

Similar flow patterns are observed in Fig. 6(c), which show images with further higher inlet qualities. However, images appear to contain more liquid than in Fig. 6(b) due to only relatively high-quality periods being captured at CHF- in Fig. 6(b). While two-phase inlet conditions preclude distinct differences between flow patterns at some inlet qualities, one clear feature that can be discerned is the movement of HDFs throughout the channel. The average velocity of the HDF as it moves through the channel is determined from the time the HDF takes to pass through the heated section of the channel ($L_h = 114.6$ mm). For example, in Fig. 6(a) the HDF passes through the channel in ~39 ms, which equates to an average HDF velocity of $\overline{u}_{HDF} = 2.9$ m/s. The HDFs

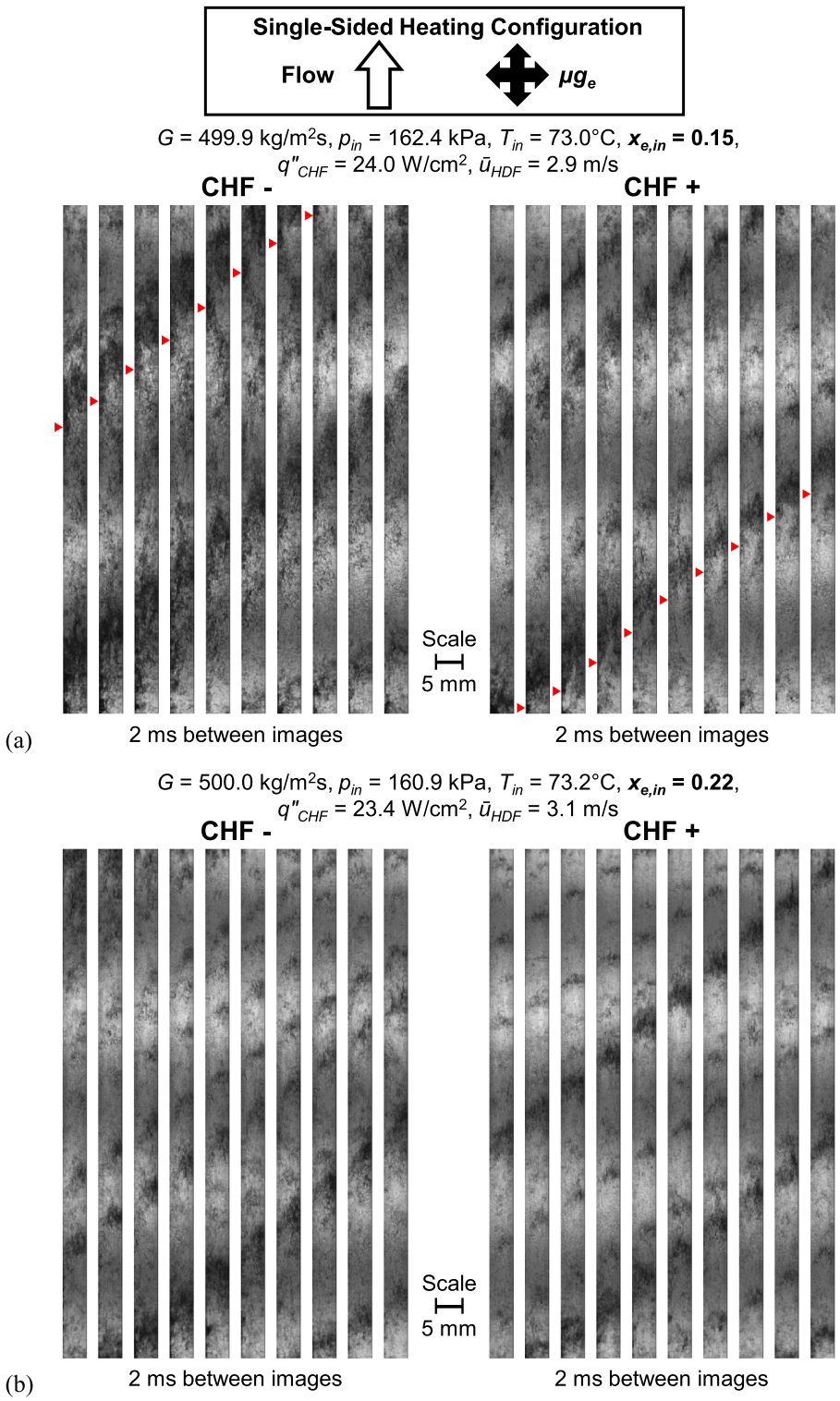

Fig. 6. Flow visualization image sequences around CHF for single-sided heating with inlet qualities of $x_{e,in}$ = (a) 0.15, (b) 0.22, (c) 0.34, (d) 0.41, and (e) 0.50 at a fixed mass velocity of $G \approx 500$ kg/m^{2}s. Time interval between successive images is mentioned below each sequence. Channel width is 5 mm.

at higher quality travel through the channel at an $\bar{u}_{HDF}$ of 3.1 and 3.7 m/s in Fig. 6(b) and (c), respectively. Further increasing inlet quality in Fig. 6 (d) and (e) result in (i) a more abrupt detachment of the trailing liquid sublayer as a HDF traverses the channel (ii) an increase in $\bar{u}_{HDF}$, corresponding to a decrease in residence time of the HDF within the channel, and (iii) a decrease in q''_{CHF}. In Fig. 6(d) and (e), the high $x_{e,in}$ produces diminutive HDFs, and significant wetting of the wall is not noticed within the channel, albeit with some attachment visible in the upstream region as soon as the HDF enters the channel.

3.2.2. *Effects of inlet pressure*

One disparity in Fig. 6(e) compared to the other subfigures in Fig. 6 is the noticeably lower inlet pressure. Fig. 7 further explores the effects of inlet pressure for both single- and double-sided heating. Two cases of

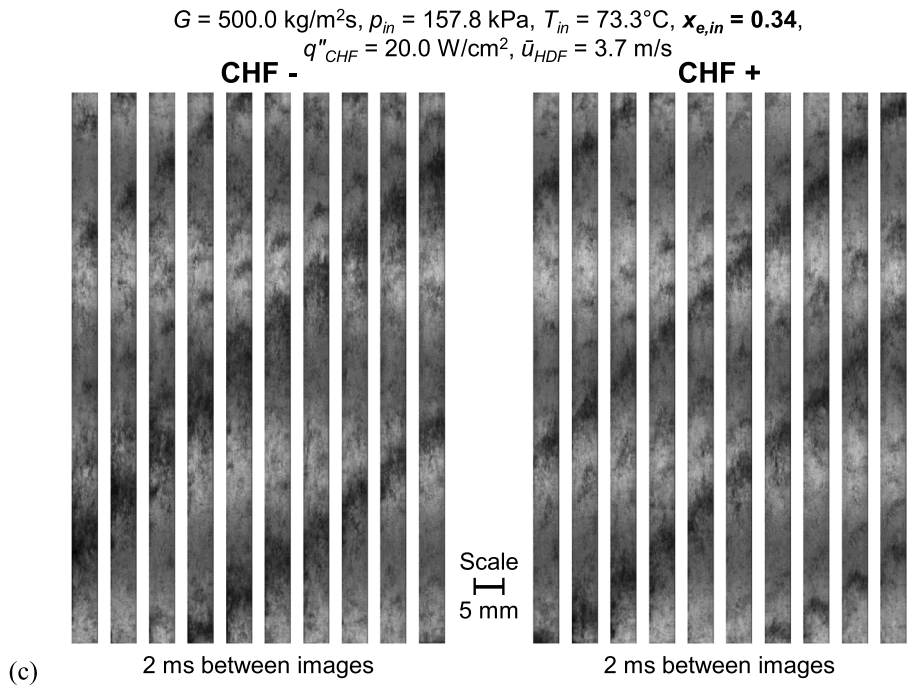

Fig. 6. (*continued*).

single-sided heating with near-identical operating conditions, but different inlet pressures, are presented in Fig. 7(a) and (b). The two pressure ranges result in nearly identical flow patterns near CHF and negligible difference in both $\overline{u}_{HDF}$, 3.2 and 3.1 m/s, and q''_{CHF}, 16.6 and 16.2 W/cm^2. Figs. 7(c) and (d) show the minor effect of pressure for double-sided heating at different operating conditions than Figs. 7(a) and (b), resulting in a drastic difference in flow patterns between the two sets of images. However, the flow patterns in Fig. 7(c) resemble those in Fig. 7(d). Overall, for the present database, p_{in} does not significantly affect flow patterns or q''_{CHF}.

3.2.3. *Effects of inlet quality for double-sided heating*

Fig. 8 features images for double-sided heating with a constant $G \approx$ 500 kg/m^{2}s but $x_{e,in}$ varied in the range of 0.09 – 0.49. The lowest inlet quality of $x_{e,in} = 0.09$ is displayed in Fig. 8(a). At both CHF- and CHF+, a HDF enters the channel, and liquid ripples exist throughout the channel, even in the high-quality downstream region. As the HDF travels downstream, boiling occurs in the residual liquid layer trailing the HDF. It should be noted that a slight tilt to the camera gives preferential viewing of the left wall. Hence, the liquid sublayer is easier to track along this wall; however, evidence of boiling is still present along the right wall where the liquid layer is lifted away from the wall due to vapor production. At CHF-, a sliver of liquid appears in the upstream region prior to a new HDF entering the channel. Conversely, at CHF+, the liquid sublayer dries up further upstream, leaving the heated wall bare and triggering CHF.

Fig. 8(b) depicts a slightly higher inlet quality of $x_{e,in} = 0.17$. At CHF-, boiling occurs within liquid film along the right wall, lifting it towards

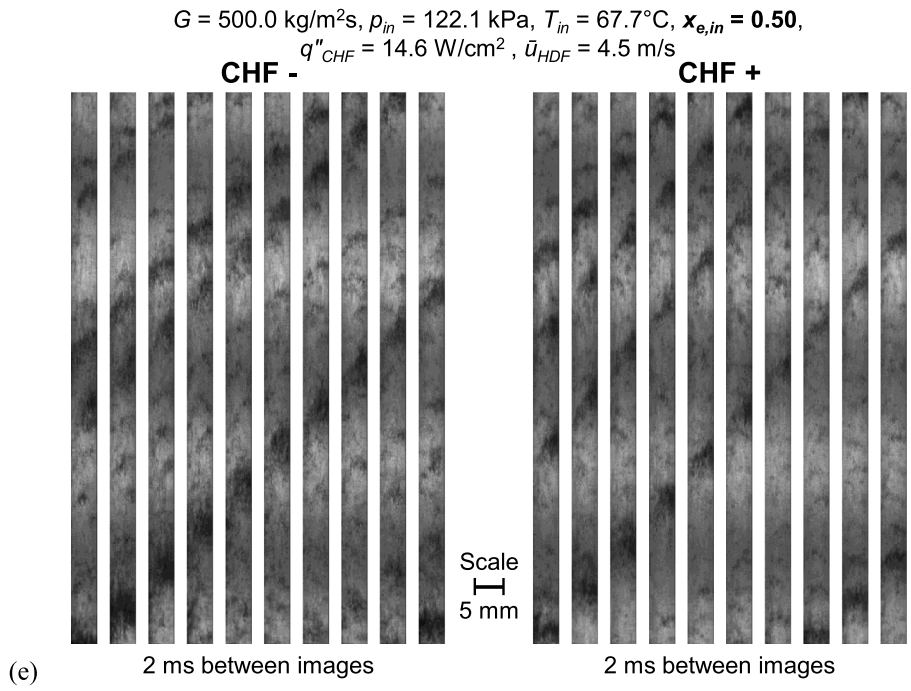

Fig. 6. (*continued*).

the core. Throughout the time sequence, boiling persists near the upstream edge. CHF is reached once the liquid contact with the heated wall cannot be maintained behind the HDF as it propagates downstream, shown at CHF+. As observed for single-sided heating in Fig. 6, increase in inlet quality from Fig. 8(a) to Fig. 8(b) resulted in an increase in $\overline{u}_{HDF}$ from 3.6 to 3.9 m/s and decrease in q''_{CHF} from 25.2 to 23.1 W/cm^2.

Similar mechanisms are observed in Fig. 8(c) and (d), corresponding to $x_{e,in}$ = 0.25 and 0.32, respectively. Increasing $x_{e,in}$ results in monotonically deteriorating q''_{CHF}, albeit at a small rate corresponding to similar $\overline{u}_{HDF}$. Further increasing the quality to $x_{e,in}$ = 0.41 lessens the influence of HDFs, and the liquid sublayer is not as prevalent along the heated walls as at lower $x_{e,in}$. This results in a relatively large decrease in q''_{CHF} and slight increase in $\overline{u}_{HDF}$ in Fig. 8(e), q''_{CHF} = 16.4 W/cm^2 and $\overline{u}_{HDF}$ = 4.4 m/s, compared to Fig. 8(d), q''_{CHF} = 20.0 W/cm^2 and $\overline{u}_{HDF}$ = 4.3 m/s, respectively. The highest inlet quality of $x_{e,in}$ = 0.49, shown in Fig. 8(f), features the lowest q''_{CHF} and highest $\overline{u}_{HDF}$. This is owed to even smaller and lighter HDFs passing quicker through the channel. Additionally, less liquid is entrained within the LDFs than at lower inlet qualities, Fig. 8(a-d), indicated by their relative clarity and uniformity.

3.3. Images at constant thermodynamic equilibrium inlet quality

Figs. 9(a-d) contain image sequences around CHF for double-sided heating with a low inlet quality, $x_{e,in}$ = 0.06 – 0.10, but at different mass velocities. Fig. 9(a) shows images for the lowest mass velocity of G = 499.9 kg/m^{2}s, also shown in Fig. 8(a). Fig. 9(b) depicts flow visualization for a slightly higher mass velocity of G = 650.4 kg/m^{2}s. As observed in the previous figures, a HDF enters the channel and boiling occurs along the wall just behind the HDF. However, at CHF+, vapor production prevents rewetting of a substantial portion of the wall upstream. Flow transients near CHF for an elevated mass velocity of G = 800.0 kg/m^{2}s are presented in Fig. 9(c). Liquid ripples are observed throughout the channel due to the increased flow inertia increasing both wall shear and turbulence and mixing liquid from the HDFs into the vapor-extensive region, darkening the images. Not only do the LDFs contain more liquid, but the HDFs are elongated compared to low inlet qualities. The spread of liquid throughout the channel aids in cooling the wall and q''_{CHF} is greater than at lower G. However, further increasing mass velocity to G = 1600.0 kg/m^{2}s, Fig. 9(d), results in an identical q''_{CHF} of 27.0 W/cm^2 as at G = 800.0 kg/m^{2}s, Fig. 9(c). This constant q''_{CHF} at high G could be due to slightly different $x_{e,in}$ in Figs. 9(c) and (d). Regardless of the difference in $x_{e,in}$, Fig. 9(d) continues the trend observed for increasing G, and liquid is now dispersed throughout the majority of the channel. Increasing the velocity of the bulk fluid also results in a corresponding increase in $\overline{u}_{HDF}$ from 3.6 m/s in Fig. 9(a) to 6.7 m/s in Fig. 9(d). The effect of G on $\overline{u}_{HDF}$ is much greater than that observed with $x_{e,in}$.

The trends in Fig. 9 are mirrored for single-sided heating at relatively high G, shown in Fig. 10. Negligible difference in q''_{CHF} was achieved irrespective of Fig. 10(a) featuring a lower G than Fig. 10(b), the latter having a more uniform liquid distribution.

Fig. 11 contains sets of images near CHF for single-sided heating with different G but at a relatively high inlet qualities of $x_{e,in}$ = 0.38 – 0.43. Analogous to the trends observed at lower $x_{e,in}$, larger G increases $\overline{u}_{HDF}$ and the presence of liquid within the LDFs. This corresponds to increasing q''_{CHF} for increasing G, shown respectively in Figs. 11(a-c). However, compared to lower inlet qualities, shown in Fig. 10, the HDFs are much shorter in length and most of the channel is occupied by a low-density mixture, even at high G, and near-wall flow features cannot be discerned. This precludes the observation of any significant differences in flow behavior between CHF- and CHF+.

4. CHF results and discussion

4.1. Parametric effects of inlet pressure, mass velocity, and inlet quality

Experimental variations of q''_{CHF} versus G for different ranges of $x_{e,in}$ are depicted in Fig. 12. The p_{in} set point in the present experiments was either 130.0 kPa (18.85 psia) or 151.7 kPa (22.00 psia). However, in order to maintain a desired constant flow rate, p_{in} was gradually increased throughout each experimental case to overcome the increased pressure drop as heat flux increased. At CHF, two different inlet pressure ranges could be identified as p_{in} < 150.0 kPa and $p_{in} \geq$ 150.0 kPa. A subset of the database with similar operating conditions in each pressure range is presented in Fig. 12(a). As shown for the significantly different sets of operating conditions shown in Fig. 12(a), the variation of p_{in} in

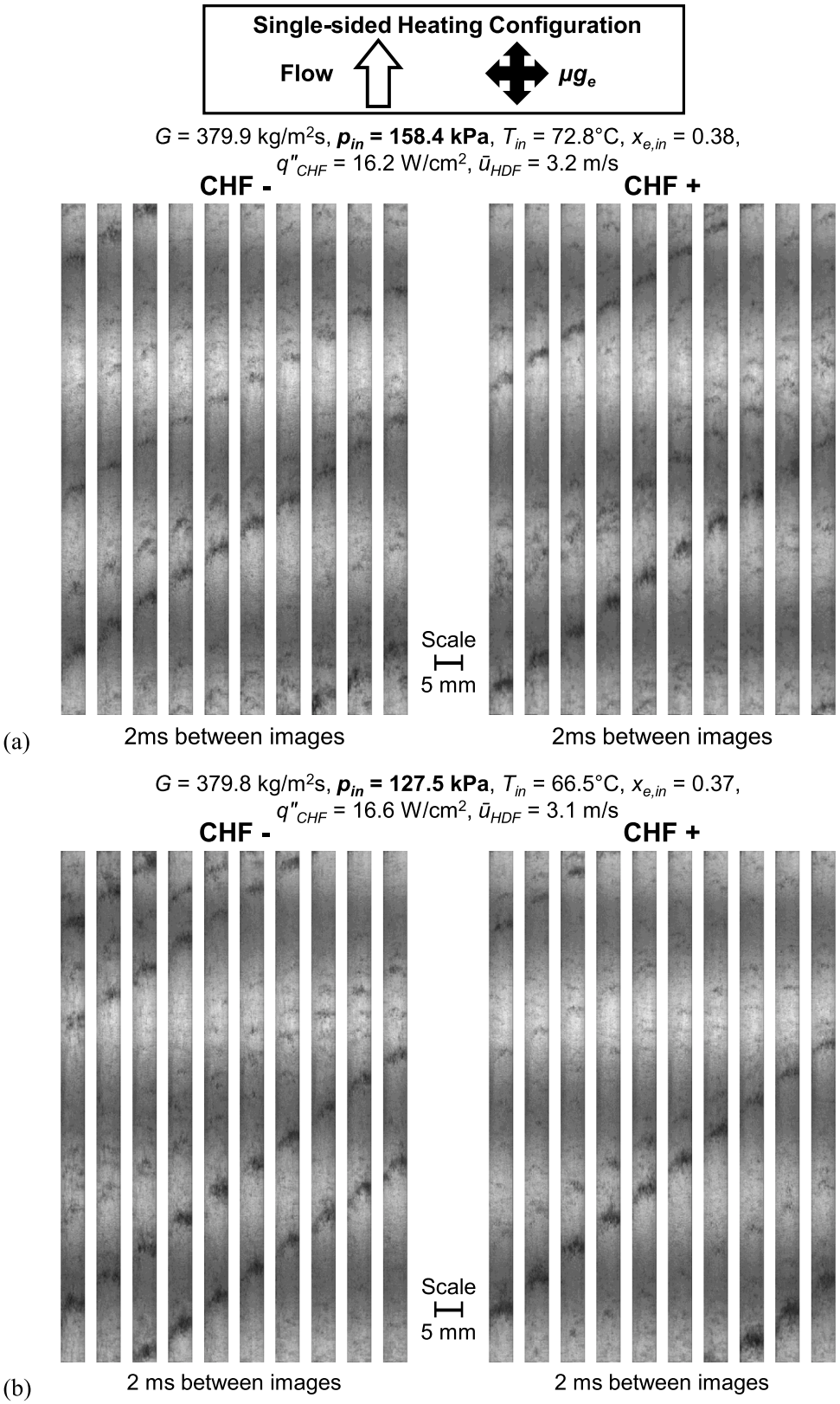

Fig. 7. Flow visualization image sequences around CHF for single-sided heating with mass velocity of $G \approx 380.0$ kg/m^{2}s and inlet quality $x_{e,in} \approx 0.38$ at inlet pressures of (a) $p_{in} = 158.4$ kPa and (b) $p_{in} = 127.5$ kPa, and double-sided heating with $G \approx 500.0$ kg/m^{2}s and $x_{e,in} \approx 0.18$ at (c) $p_{in} = 167.7$ kPa and (d) $p_{in} = 135.2$ kPa. Time interval between successive images is mentioned below each sequence. Channel width is 5 mm.

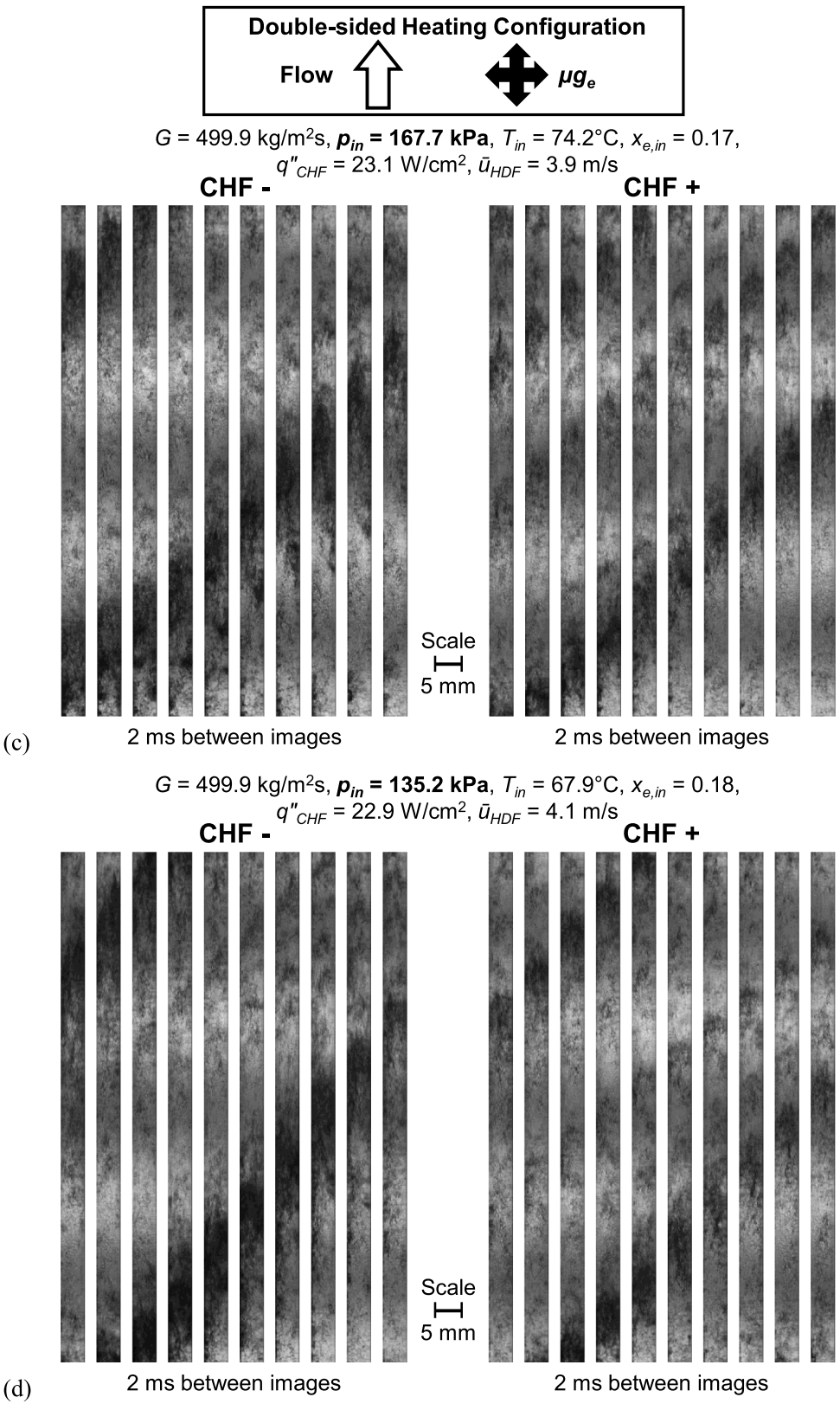

Fig. 7. (*continued*).

the present database has a relatively mild influence on q''_{CHF}. For this reason, the ensuing figures will focus on more dominant trends and will not distinguish between p_{in} ranges.

Figs. 12(b) and (c) show results for the entire database with single- and double-sided heating, respectively. Practically, the range of inlet qualities obtainable at each G were limited by (i) the sonic limit of the FBM and (ii) inherent operation of the BHM heaters during cases with two-phase inlet. Consequently, fine increments in $x_{e,in}$ was not possible for broad ranges of G, as they were for subcooled inlet [34], and hence CHF data could not be obtained for several combinations of operating

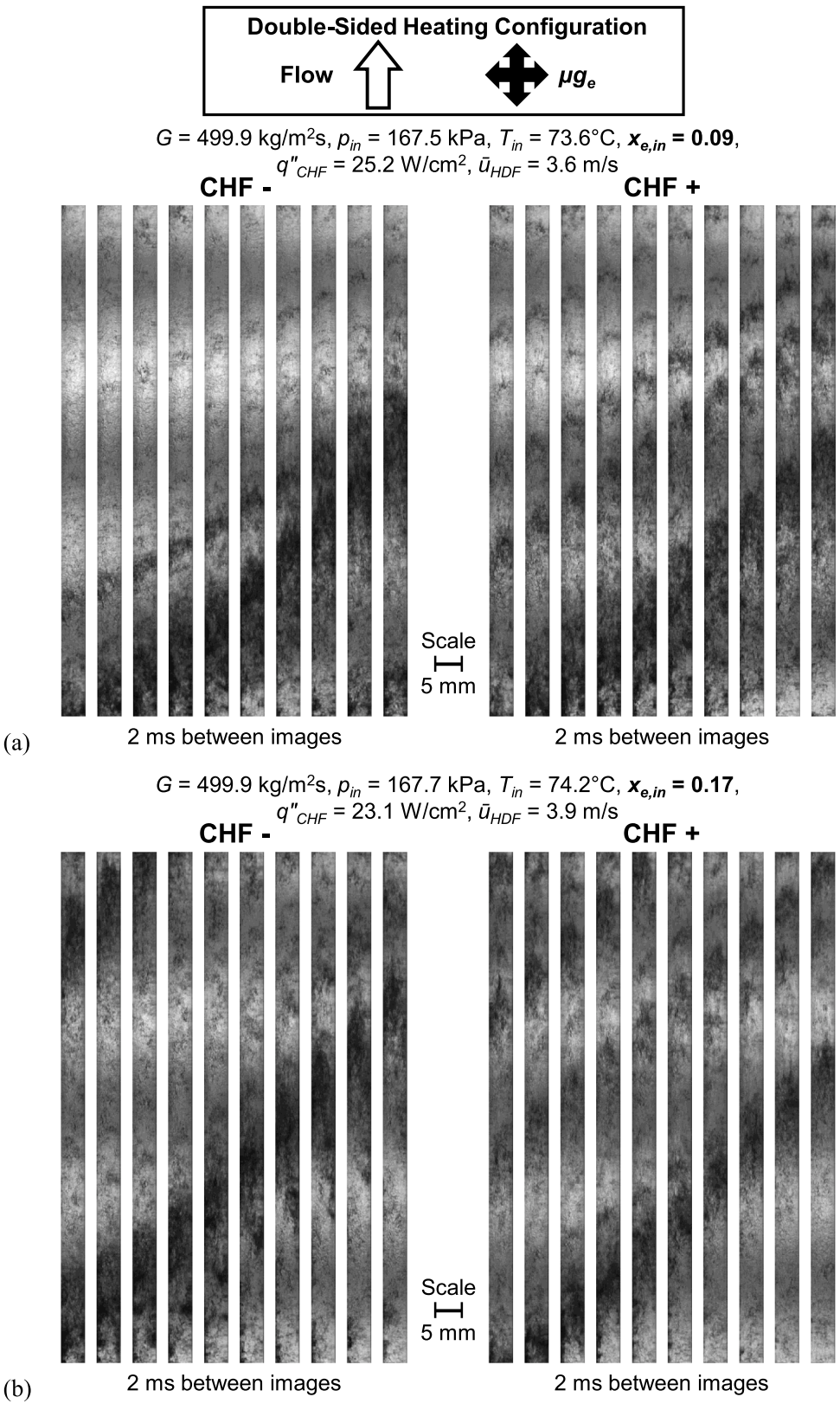

Fig. 8. Flow visualization image sequences around CHF for double-sided heating with inlet qualities of $x_{e,in}$ = (a) 0.09, (b) 0.17, (c) 0.25, (d) 0.32, (e) 0.41, and (f) 0.45 at a fixed mass velocity of $G \approx 500$ kg/m^{2}s. Time interval between successive images is mentioned below each sequence. Channel width is 5 mm.

conditions. The majority of data was obtained for $G \leq 790$ kg/m^{2}s across an extensive range of inlet qualities. In this range, q''_{CHF} increases with increasing G and/or decreasing $x_{e,in}$. Higher mass velocities of $G \geq 790$ kg/m^{2}s were only achievable at relatively low inlet qualities and resulted in constant q''_{CHF}. This is attributed to the diminished q''_{CHF} enhancement upon increasing G at high mass velocities coupled with

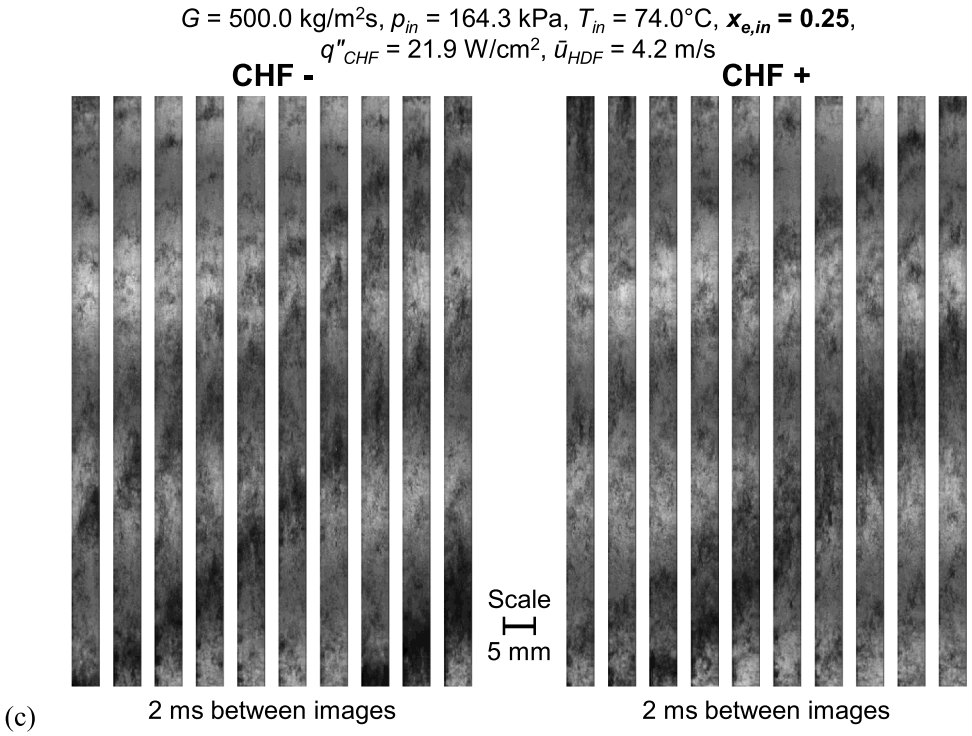

(c)

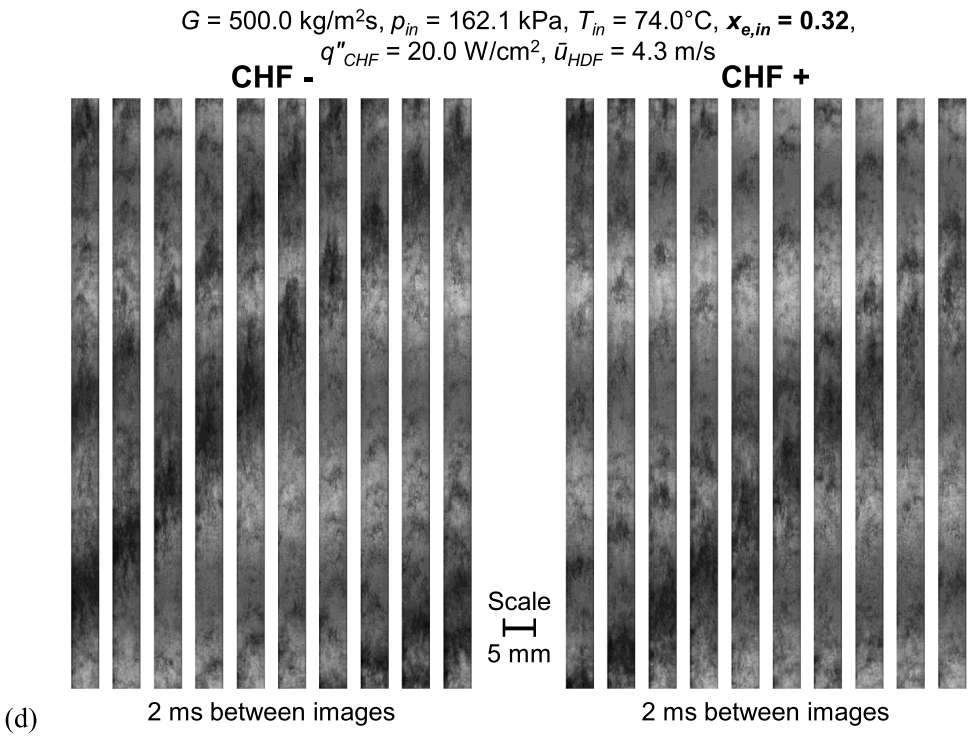

(d)

Fig. 8. (*continued*).

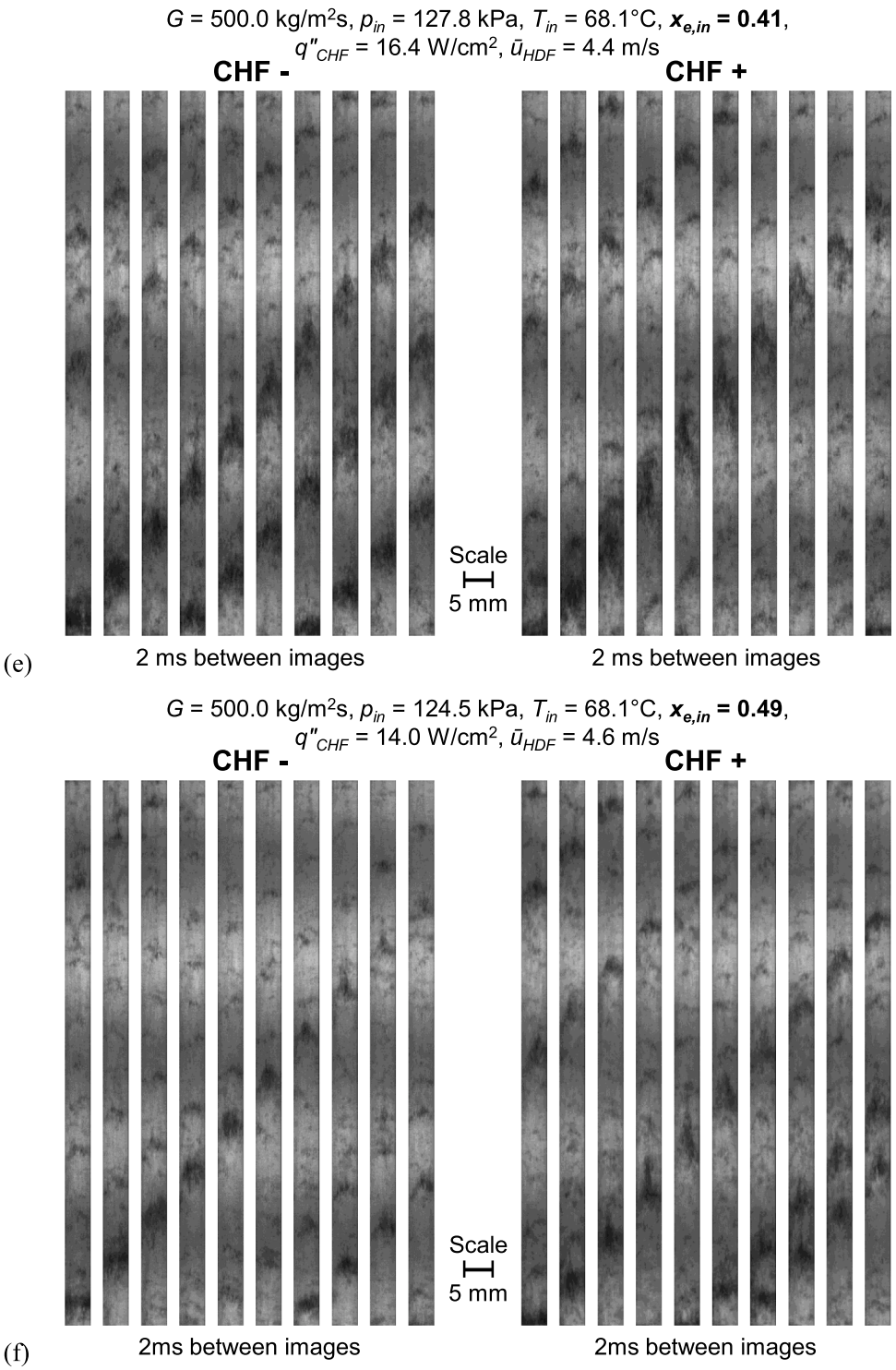

Fig. 8. (*continued*).

variations in $x_{e,in}$.

The influence of inlet quality is further explored in Figs. 13(a) and (b), which show plots of q''_{CHF} versus $x_{e,in}$ for different ranges of G during single- and double-sided heating, respectively. For both heating configurations, q''_{CHF} decreases almost linearly upon increasing $x_{e,in}$ irrespective of G or heating configuration. An exception to the monotonic behavior is seen at very low inlet qualities, near saturation. For $G = 790$ kg/m^{2}s, q''_{CHF} initially increases with increasing $x_{e,in}$, before decreasing. This trend was in fact already observed in Earth gravity [31]. Fig. 13(c) overlays q''_{CHF} for both single- and double-sided heating with similar operating conditions on the same plot. Heating configuration does not strongly influence q''_{CHF} for two-phase inlet, as opposed to subcooled inlet [33,34]. Identical trends are reflected in plots of q''_{CHF} versus $x_{e,out}$ in Figs. 14(a) and (b) for single- and double-sided heating, respectively. However, CHF occurs at a higher $x_{e,out}$ for double-sided heating than single-sided for equivalent inlet conditions due to double-sided heating having twice the heating area and similar q''_{CHF} yielding greater fluid enthalpy gain.

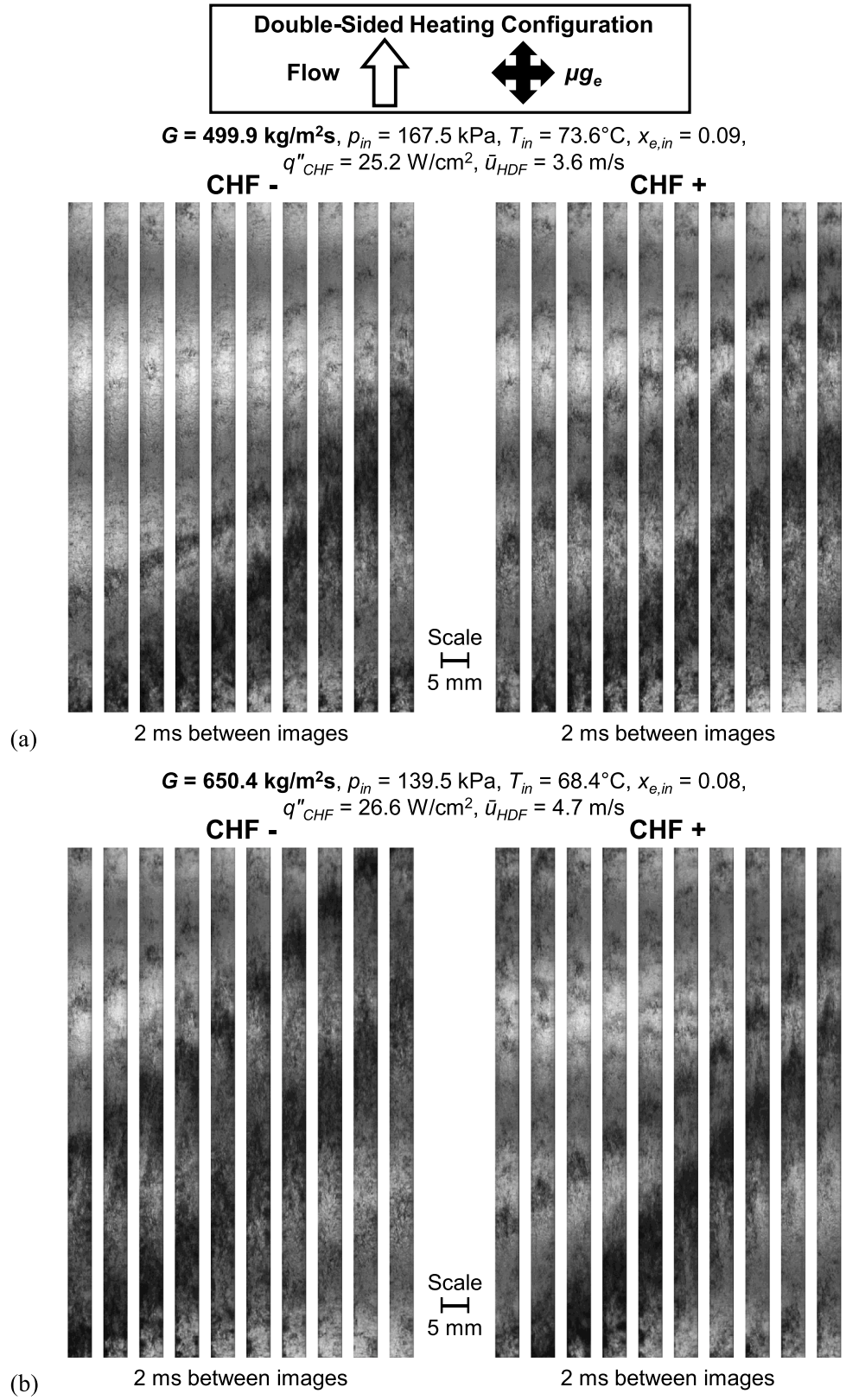

Fig. 9. Flow visualization image sequences around CHF for double-sided heating with mass velocities of G = (a) 499.9, (b) 650.4, (c) 800.0, and (d) 1600.0 kg/m^{2}s at a fixed inlet quality of $x_{e,in} \approx 0.08$. Time interval between successive images is mentioned below each sequence. Channel width is 5 mm.

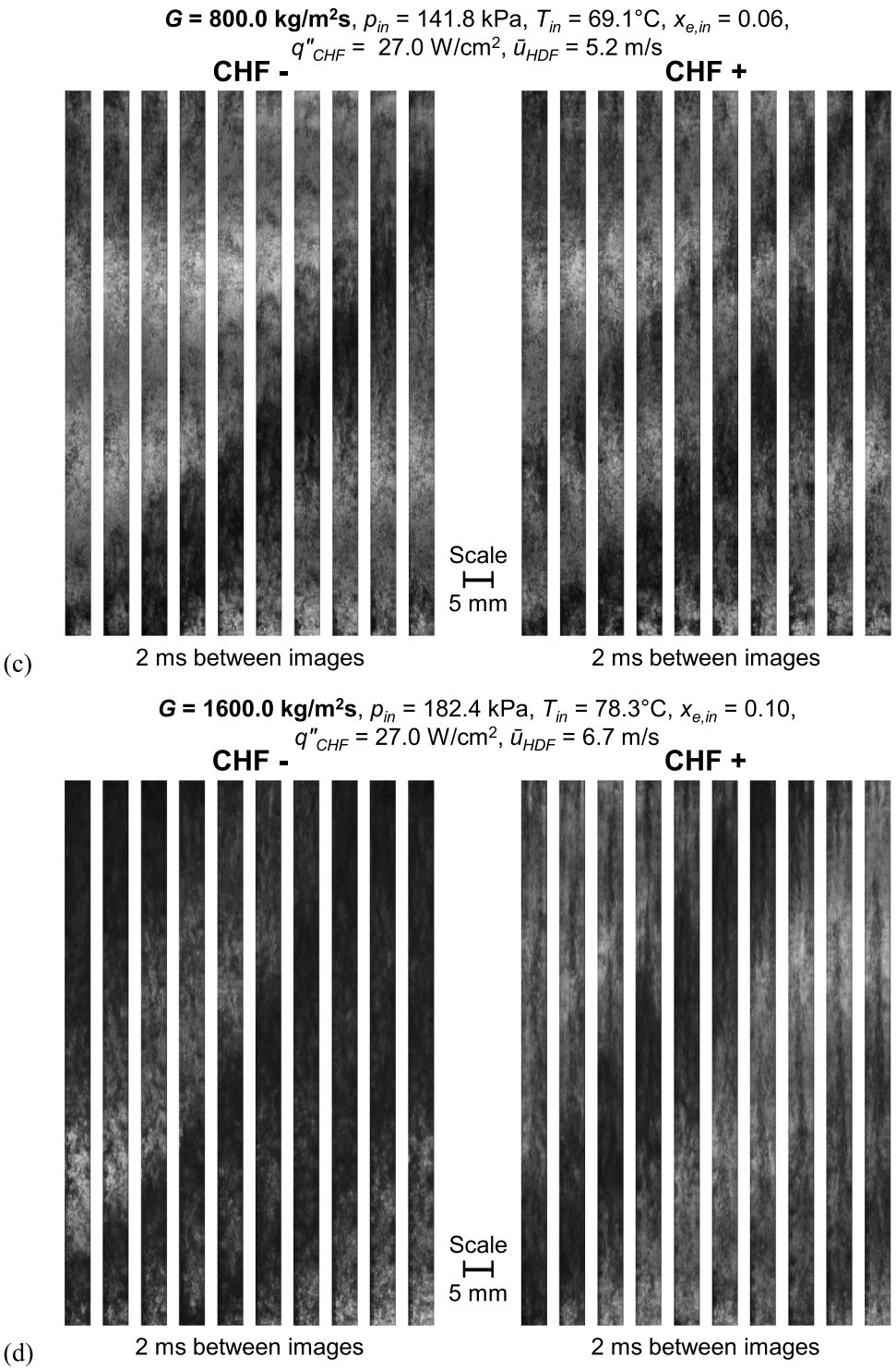

Fig. 9. (*continued*).

4.2. Dimensionless group relationships

The vertical axis is non-dimensionalized by transforming q''_{CHF} to *Bo* in Fig. 15. Fig. 15(a) and (b) show *Bo* versus $x_{e,in}$ for single- and double-sided heating, respectively. Increasing *G* results in lower *Bo,* and for each mass velocity, *Bo* linearly decreases with increasing $x_{e,in}$. Fig. 15(c) and (d) show plots for *Bo* versus $x_{e,out}$. Similar to the shift observed between the dimensional results in Figs. 13 and 14, the trends of *Bo* versus $x_{e,in}$ are preserved but translated to higher qualities when plotted versus $x_{e,out}$, especially for double-sided heating.

The effects of q''_{CHF} can be emphasized by using the dimensionless term Bo^2We_D, which consists of q''_{CHF} and various fluid properties. Fig. 16 depicts plots of Bo^2We_D versus $x_{e,in}$ and $x_{e,out}$ for both single- and double-sided heating. The spread of the data with respect to *G* observed in Fig. 15 has now collapsed into a single near-linear trend. This replicates the trends observed in the dimensional plots of q''_{CHF} versus $x_{e,in}$ and $x_{e,out}$. Similar non-dimensionalization is performed for *G* and the results shown in Fig. 17. For both single- and double-sided heating, plots of Bo^2We_D versus Re_{fo} are displayed in Fig. 17(a) and (b), respectively. While only previously established trends are observed in these non-

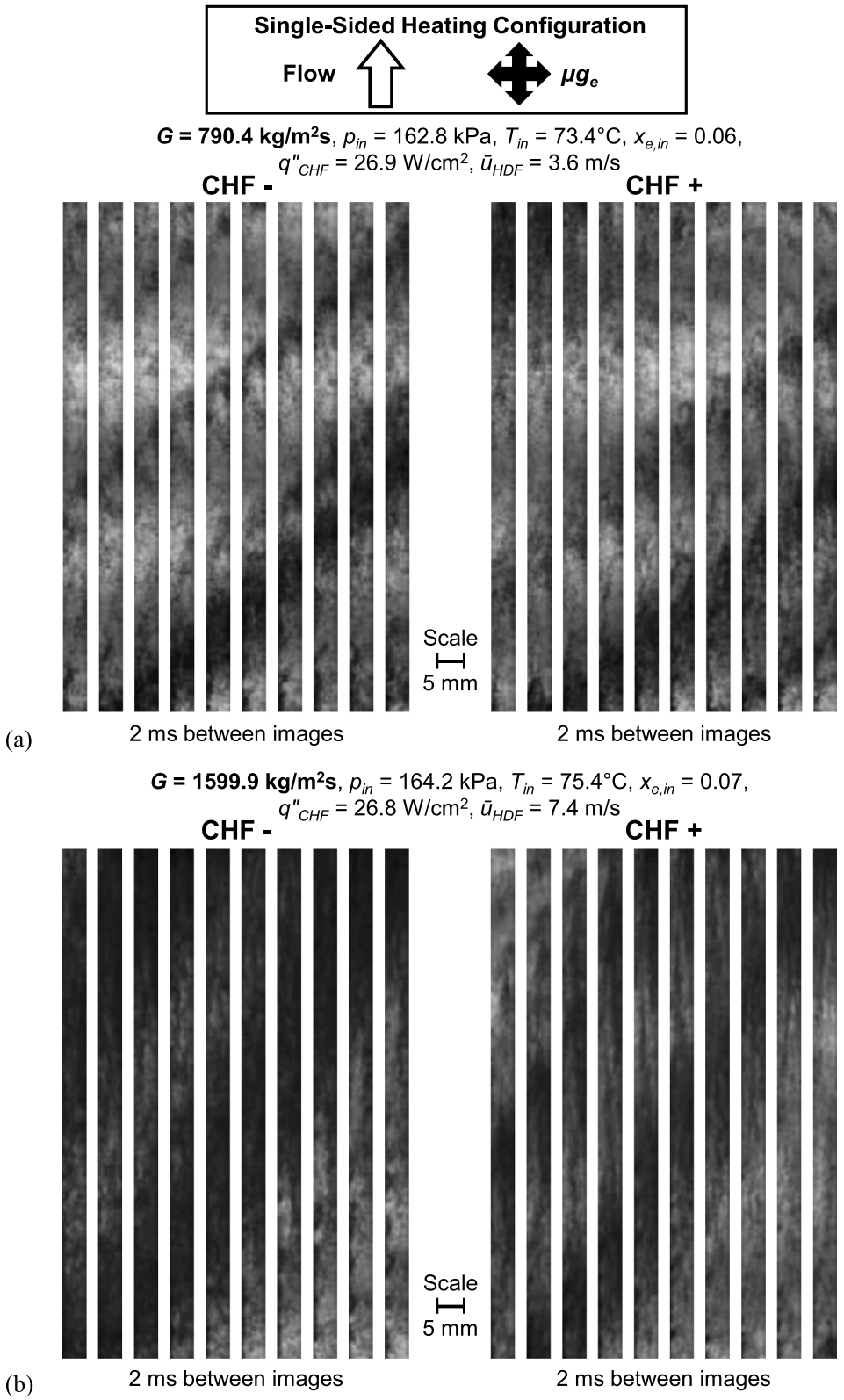

Fig. 10. Flow visualization image sequences around CHF for single-sided heating with mass velocities of G = (a) 790.4 and (b) 1599.9 kg/m^{2}s at a fixed inlet quality of $x_{e,in} \approx 0.07$. Time interval between successive images is mentioned below each sequence. Channel width is 5 mm.

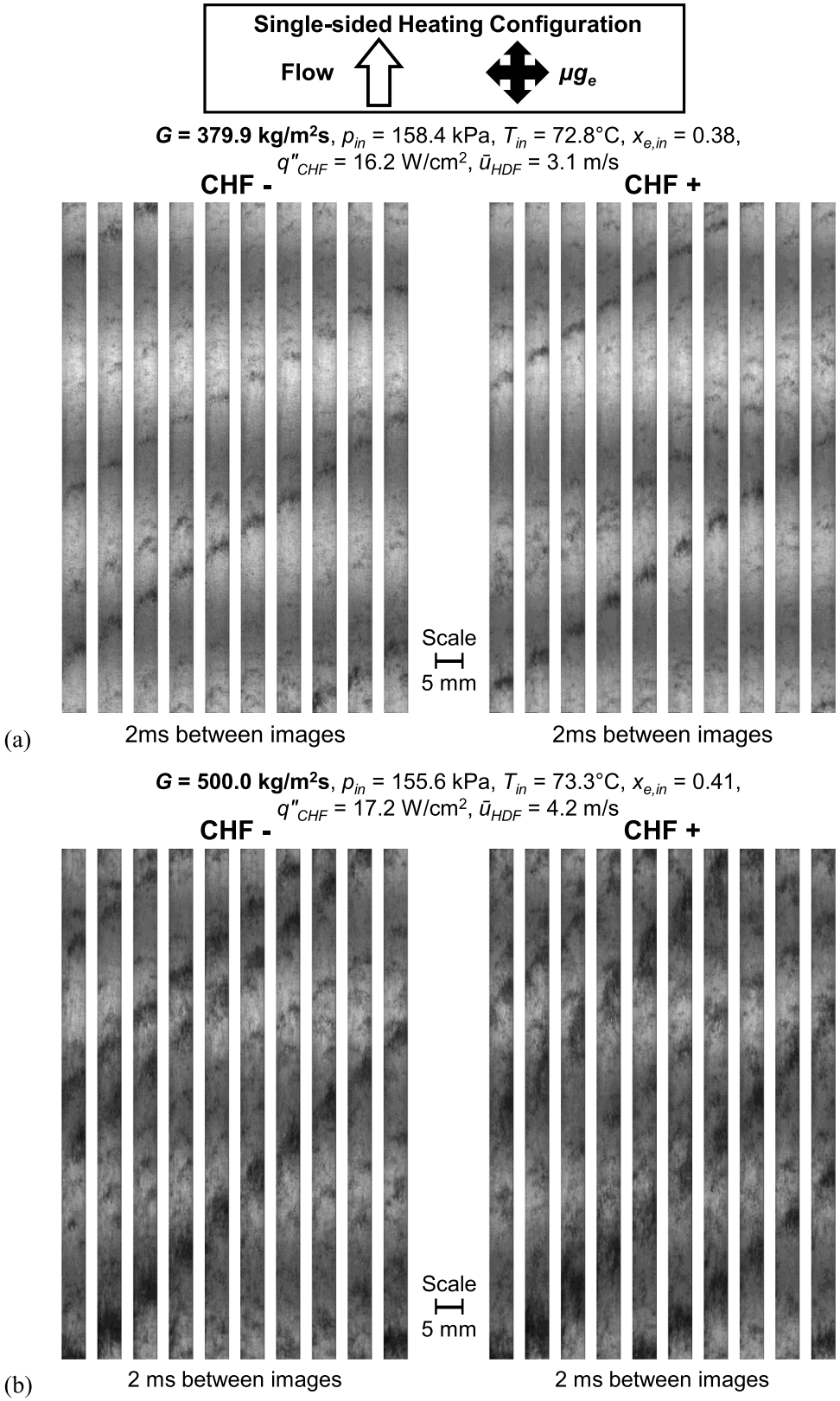

Fig. 11. Flow visualization image sequences around CHF for single-sided heating with mass velocities of G = (a) 379.9, (b) 500.0, and (c) 790.3 kg/m^{2}s at a fixed inlet quality of $x_{e,in} \approx 0.40$. Time interval between successive images is mentioned below each sequence. Channel width is 5 mm.

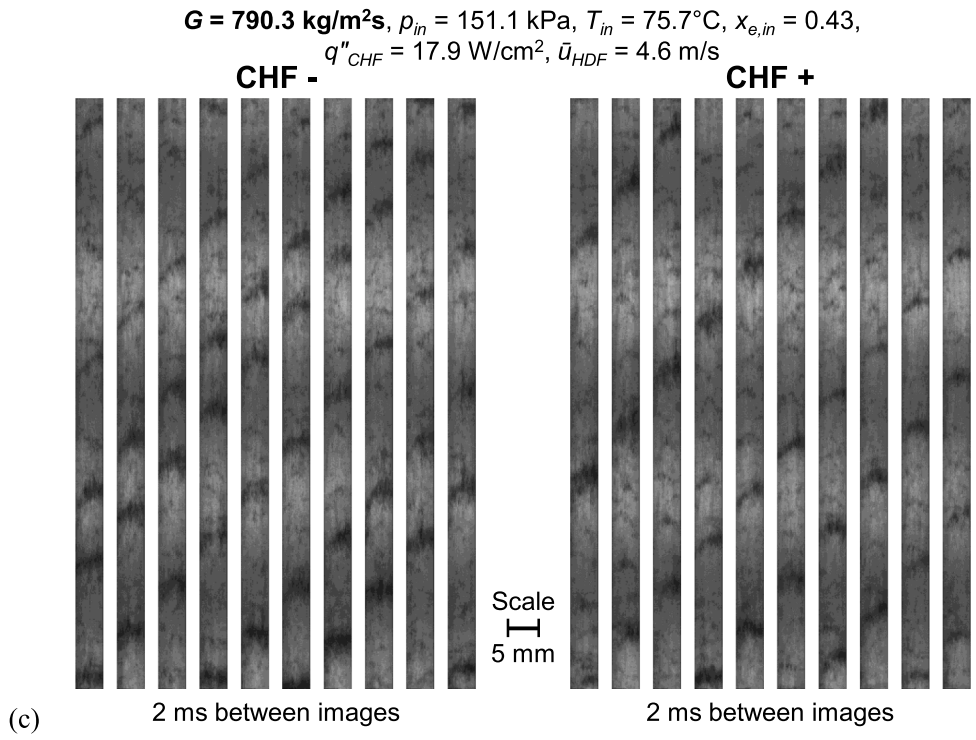

Fig. 11. (*continued*).

dimensional plots, dimensionless results allow easy comparison to other databases and function as inputs into many common correlations.

4.3. Comparison to earth gravity data

Fig. 18 compares the q''_{CHF} data collected in microgravity (ISS experiments) to those collected in the vertical upflow orientation in Earth gravity prior to launch during (MST experiments). The MST experiments were performed for a subset of the ISS experiment matrix [31]. Results for similar operating conditions in the two gravity environments are presented as a plot of q''_{CHF} versus G, traditionally used to show the mitigating effects of gravity as flow inertia increases. However, for the two-phase inlet cases presented in Fig. 18(a), strong effects of inertia and interfacial shear stress, attributed to the considerable amount of vapor throughout the channel, dampen the influence of g, even at relatively low flow rates. This trend is observed for both heating configurations, unlike subcooled inlet [34], presented in Fig. 18(b) and (c), respectively for single- and double-sided heating. Similar to the trend for two-phase inlet, flow acceleration due to additional vapor production in double-sided heating negated the lack of gravity. However, q''_{CHF} degraded in μg_e during single-sided heating with subcooled inlet, where buoyancy significantly aided vapor removal from the channel during vertical upflow in $1g_e$.

5. CHF prediction tools

5.1. Interfacial lift-off model

5.1.1. Model description

Careful examination of the near-wall behavior at CHF in section 3.1 reveals the presence of a wavy liquid-vapor interface described in *the Interfacial Lift-off Model*. Although originally developed by Galloway and Mudawar [46], the model has previously been used to good effect for a variety of inlet conditions, heating configurations, and gravitational environments [31,38,47]. The model assumes, prior to CHF, cooling of the heated wall primarily occurs at troughs in the interface between the liquid and wavy vapor layer which forms along the heated wall. The troughs, called *wetting fronts*, allow liquid to access the heated wall and facilitate boiling as they slide along the wall. CHF is hypothesized to occur when the momentum (normal to the heated wall) of vapor produced in the wetting front overcomes the pressure force exerted by the liquid-vapor interface, causing the wetting front to lift off the heated wall. At this point, liquid loses contact with the wall and heat that was being removed at the now-detached wetting front transfers axially to upstream wetting fronts. This results in a chain-reaction-like detachment of consecutive wetting fronts until the entire wall is blanketed by vapor. The adaptation of the *Interfacial Lift-off Model* by Kharangate *et al.* [38] accounts for two-phase inlet conditions and is employed in the present study. An idealized schematic of the modeled flow pattern for double-sided heating is depicted in Fig. 19. For the present μg_e database, gravitational acceleration is negligible and $g = 0$, rendering the terms containing the channel orientation, θ, irrelevant. An abridged description of the model is provided, and further details of the model, including its applicability in $1g_e$, can be found in [38].

Four sub-models serve as building blocks for the *Interfacial Lift-off Model*. A separated flow model predicts axial variations in pressure, phase velocities, quality, and void fraction, which serve as inputs for the other three sub-models. As shown in Fig. 19, an annular flow is assumed to enter the channel with a central vapor core and outer liquid layer covering the walls. Upon reaching the heated length, a wavy vapor layer forms on each heated wall, with a thin liquid layer remaining between it and the vapor core. In the case of single-sided heating, a wavy vapor layer forms at the heated wall while the opposite adiabatic wall remains covered with liquid. The following assumptions are applied during the separated flow model:

(i) Wavy vapor layers are initiated at the leading edge of the heated walls.
(ii) The vapor core has constant quality along the channel.
(iii) The velocity of each phase is uniform across the channel's cross section.
(iv) Pressure is uniform across the channel's entire cross section.
(v) Each phase remains at the local saturation temperature.

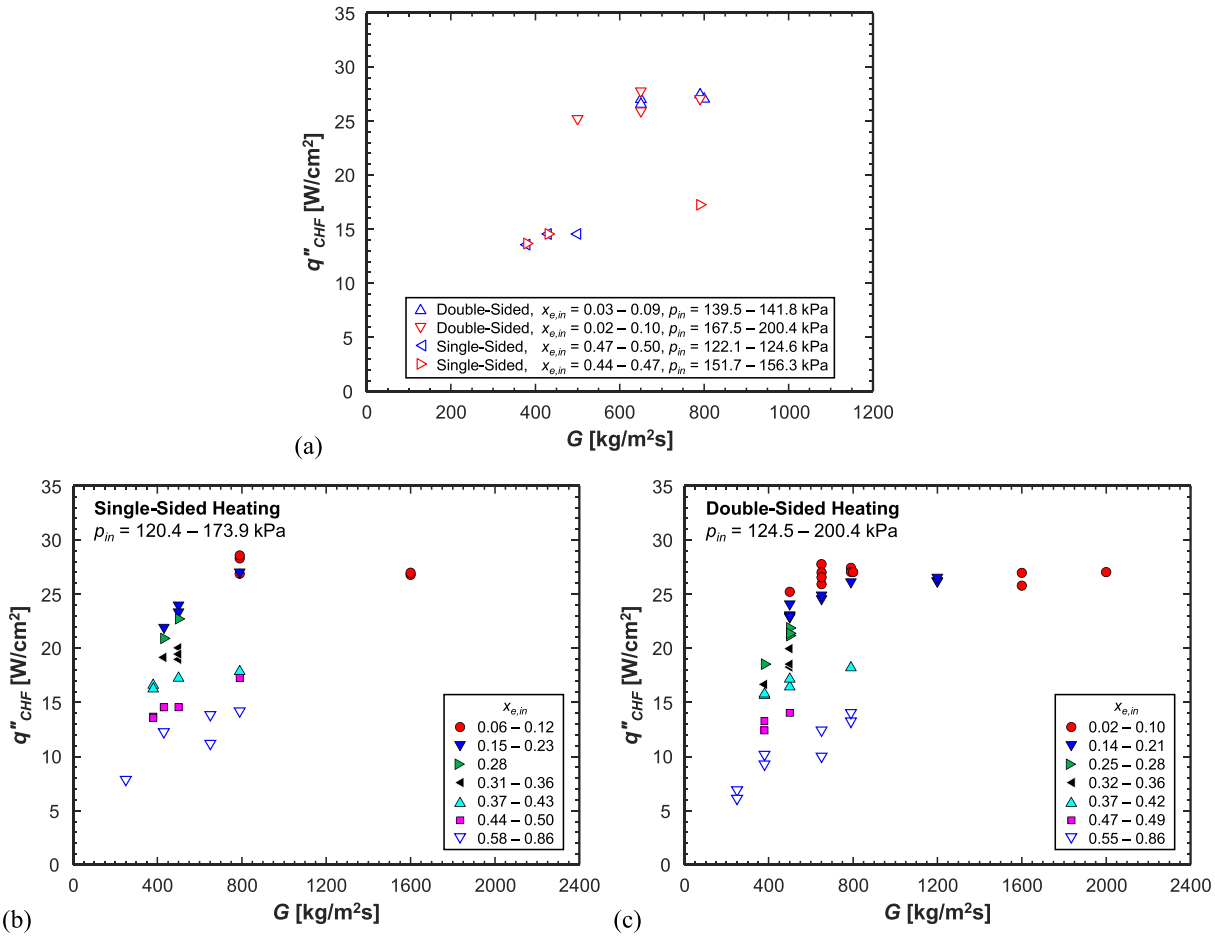

Fig. 12. Variations of experimental CHF, q''_{CHF}, versus mass velocity, G, for (a) a subset of the database at different ranges of inlet pressure, p_{in}, and for the entire database with (b) single- and (c) double-sided heating. In plots (b) and (c), the datapoints are segregated into several bands of inlet quality, $x_{e,in}$, for the entire range of inlet pressure, p_{in}.

(vi) Vapor produced at the wetting front does not contribute to streamwise momentum, and,
(vii) For double-sided heating, the heat flux supplied by each heated wall is equal and uniform.

Eqs. (4)-(6), (7), (8) and (9)-(10) present the resulting key equations for conservation of mass, momentum during single-sided heating, momentum during double-sided heating, and energy, respectively.

$$u_{ga} = \frac{x_a G}{\rho_g \alpha_a} \tag{4}$$

$$u_{co} = \frac{x_{co} G}{\rho_g \alpha_{co}} \tag{5}$$

$$u_f = \begin{cases} \dfrac{(1 - x_{co} - x_1)G}{(1 - \alpha_{co} - \alpha_1)\rho_f}, & \text{single – sided} \\ \dfrac{(1 - x_{co} - x_1 - x_2)G}{(1 - \alpha_{co} - \alpha_1 - \alpha_2)\rho_f}, & \text{double – sided} \end{cases} \tag{6}$$

$$\left.\begin{aligned} G^2 \frac{d}{dz}\left[\frac{x_{co}^2}{\rho_g \alpha_{co}}\right] &= -\alpha_{co}\frac{dp}{dz} \pm \frac{\tau_{i,co} P_{i,co}}{A_c} - \rho_g \alpha_{co} g \sin\theta && \text{vapor core} \\ G^2 \frac{d}{dz}\left[\frac{x_1^2}{\rho_g \alpha_1}\right] &= -\alpha_1\frac{dp}{dz} - \frac{\tau_{w1,g} P_{w1,g}}{A_c} \pm \frac{\tau_{i,1} P_{i,1}}{A_c} - \rho_g \alpha_1 g \sin\theta && \text{vapor layer} \\ G^2 \frac{d}{dz}\left[\frac{(1 - x_{co} - x_1)^2}{\rho_f (1 - \alpha_{co} - \alpha_1)}\right] &= -(1 - \alpha_{co} - \alpha_1)\frac{dp}{dz} - \frac{\tau_{wf} P_{wf}}{A_c} \mp \frac{\tau_{i,co} P_{i,co}}{A_c} \mp \frac{\tau_{i,1} P_{i,1}}{A_c} - \rho_f (1 - \alpha_{co} - \alpha_1) g \sin\theta && \text{liquid film} \end{aligned}\right\} \tag{7}$$

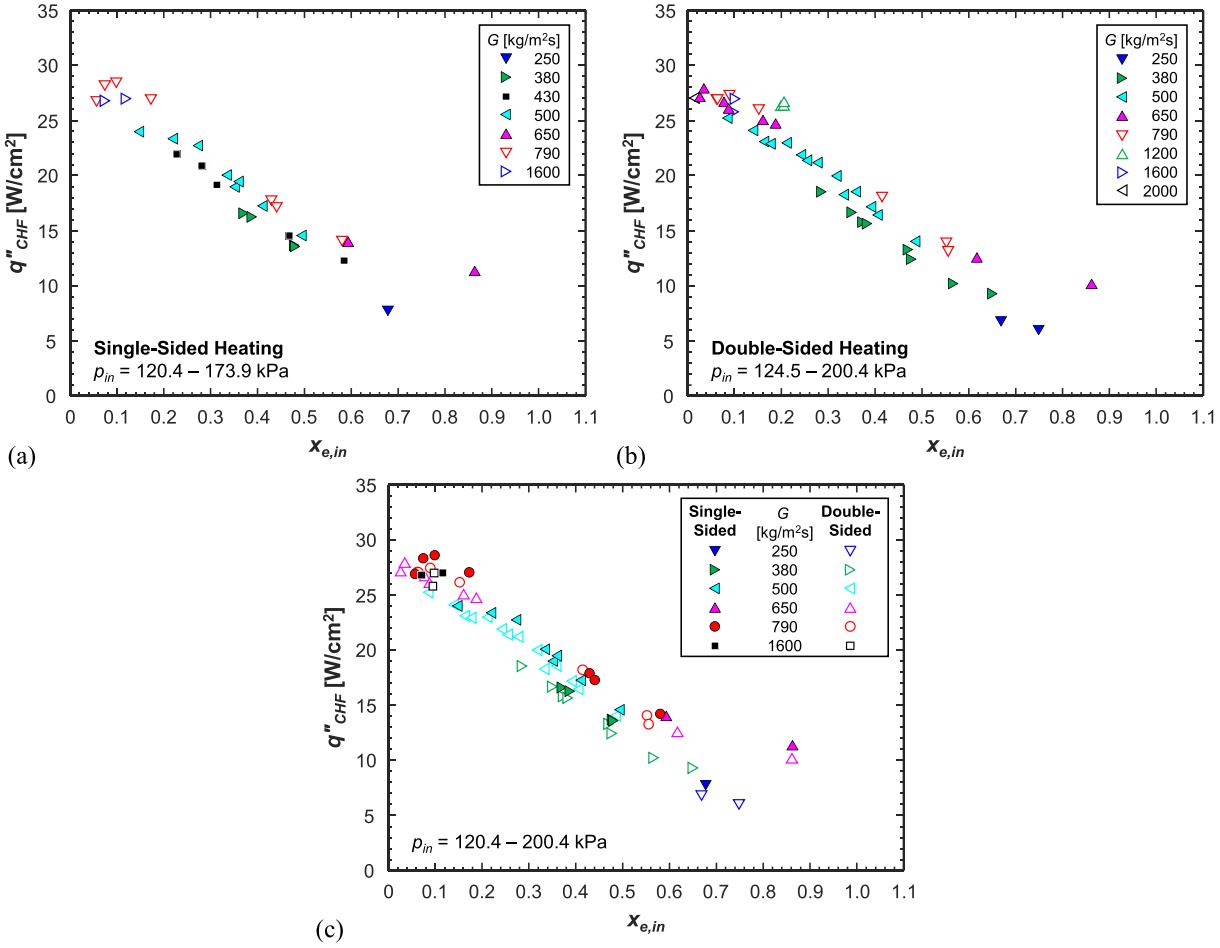

Fig. 13. Variations of experimental CHF, q''_{CHF}, versus mass velocity, G, for (a) single-sided heating, (b) double-sided heating, and (c) both heating configurations combined. In each plot, for the entire range of inlet pressure, p_{in}, the datapoints are segregated by mass velocity in the range of G = 250 – 2000 kg/m^{2}s.

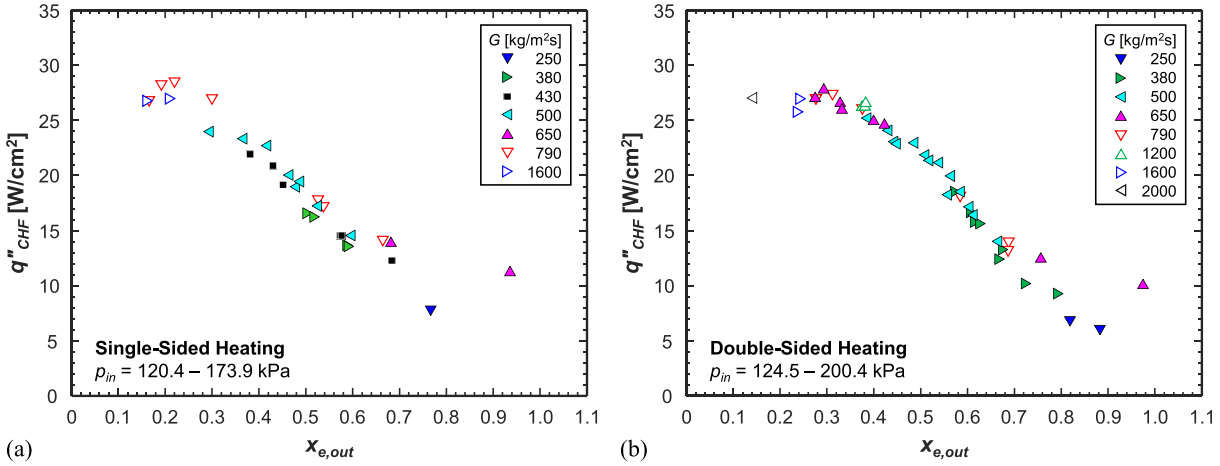

Fig. 14. Variations of experimental CHF, q''_{CHF}, versus outlet quality, $x_{e,out}$, for (a) single- and (b) double-sided heating. In each plot, for the entire range of inlet pressure, p_{in}, the datapoints are segregated by mass velocity in the range of G = 250 – 2000 kg/m^{2}s.

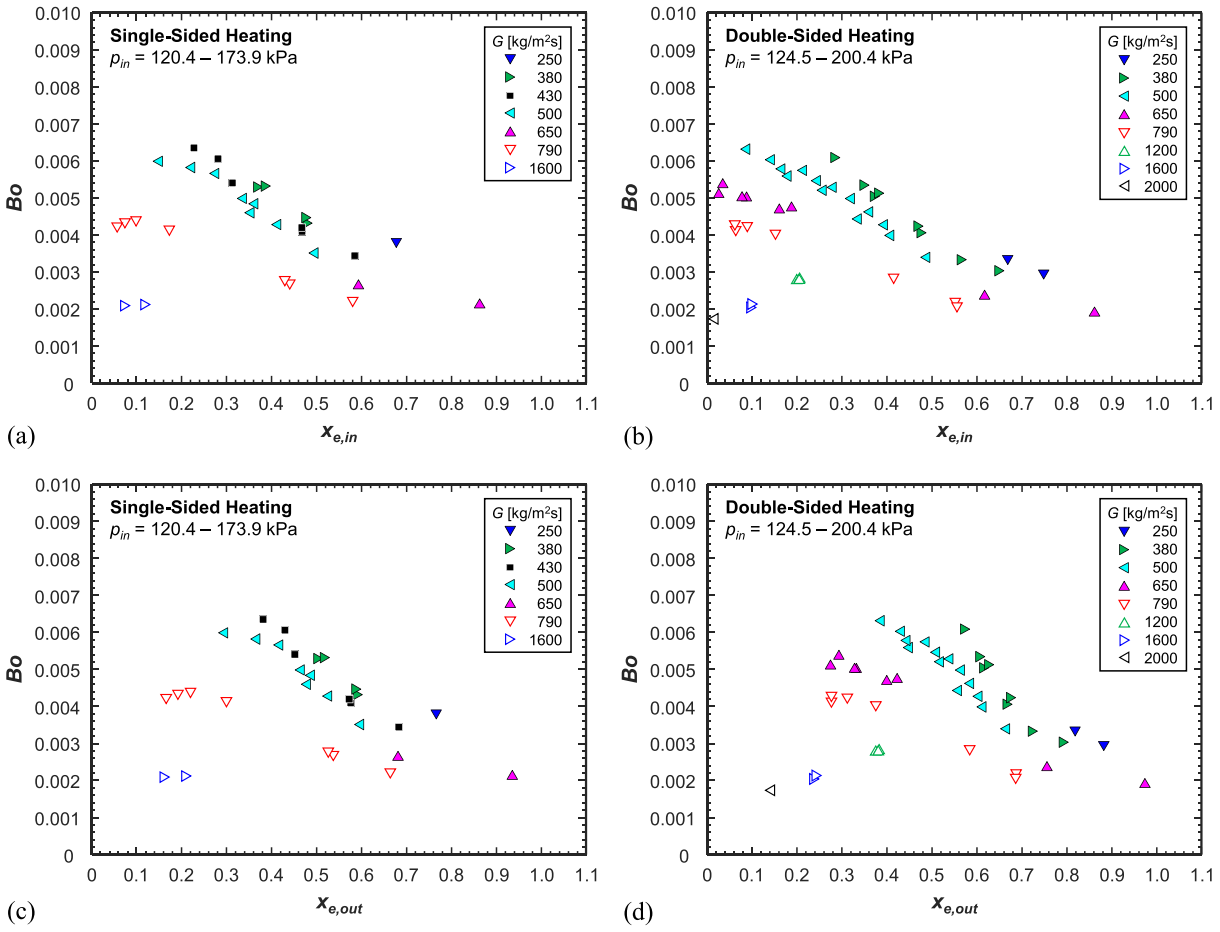

Fig. 15. Variations of boiling number, *Bo*, versus inlet quality, $x_{e,in}$, for (a) single- and (b) double-sided heating, and *Bo* versus outlet quality, $x_{e,out}$, for (c) single- and (d) double-sided heating. In each plot, for the entire range of inlet pressure, p_{in}, the datapoints are segregated by mass velocity in the range of $G = 250 - 2000$ kg/m^{2}s.

$$
\begin{aligned}
G^2\frac{d}{dz}\left[\frac{x_{co}^2}{\rho_g\alpha_{co}}\right] &= -\alpha_{co}\frac{dp}{dz} \pm \frac{\tau_{i,co}P_{i,co}}{A_c} - \rho_g\alpha_{co}g\sin\theta && \text{vapor core}\\
G^2\frac{d}{dz}\left[\frac{x_1^2}{\rho_g\alpha_1}\right] &= -\alpha_1\frac{dp}{dz} - \frac{\tau_{w1,g}P_{w1,g}}{A_c} \pm \frac{\tau_{i,1}P_{i,1}}{A_c} - \rho_g\alpha_1 g\sin\theta && \text{vapor layer 1}\\
G^2\frac{d}{dz}\left[\frac{x_2^2}{\rho_g\alpha_2}\right] &= -\alpha_2\frac{dp}{dz} - \frac{\tau_{w2,g}P_{w2,g}}{A_c} \pm \frac{\tau_{i,2}P_{i,2}}{A_c} - \rho_g\alpha_2 g\sin\theta && \text{vapor layer 2}\\
G^2\frac{d}{dz}\left[\frac{(1-x_{co}-x_1-x_2)^2}{\rho_f(1-\alpha_{co}-\alpha_1-\alpha_2)}\right] &= -(1-\alpha_{co}-\alpha_1-\alpha_2)\frac{dp}{dz} - \frac{\tau_{w,f}P_{w,f}}{A_c} \mp \frac{\tau_{i,co}P_{i,co}}{A_c} \mp \frac{\tau_{i,1}P_{i,1}}{A_c} \mp \frac{\tau_{i,2}P_{i,2}}{A_c} - \rho_f(1-\alpha_{co}-\alpha_1-\alpha_2)g\sin\theta && \text{liquid film}
\end{aligned}
\tag{8}
$$

$$\frac{dx_{co}}{dz} = 0 \tag{9}$$

$$\frac{dx_a}{dz} = \frac{q''_w W}{GAh_{fg}} \tag{10}$$

The wall and interfacial shear stress terms are determined by Eqs. (11) and (12), respectively,

$$\tau_{w,k} = \frac{1}{2}\rho_k u_k f_k \text{ and} \tag{11}$$

$$\tau_{ia} = C_{f,a}\rho_g\left(u_{ga} - u_f\right)^2, \tag{12}$$

where $C_{f,a} = 0.5$ [46] and the phase friction factor is determined via Eq. (13) as prescribed by Bhatti and Shah [48].

$$f_k = C_1 + \frac{C_2}{Re_k^{1/C_3}}, \begin{cases} C_1 = 0;\ C_2 = 16;\ C_3 = 1, & Re_k \le 2100 \\ C_1 = 0.0054;\ C_2 = 2.3\times10^{-8};\ C_3 = -2/3, & 2100 < Re_k \le 4000 \\ C_1 = 0.00128;\ C_2 = 0.1143;\ C_3 = 3.2154, & Re_k > 4000 \end{cases} \tag{13}$$

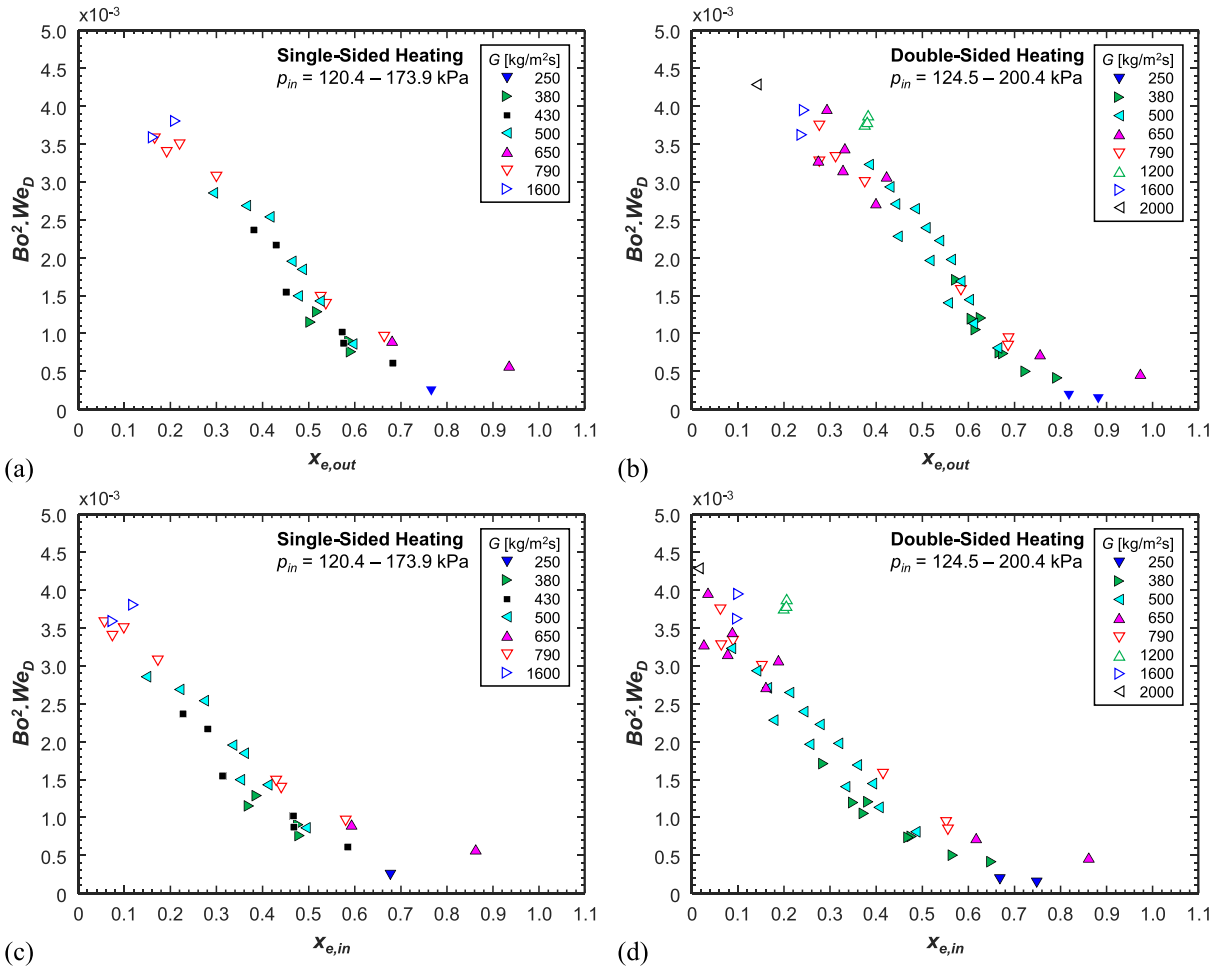

Fig. 16. Variations of dimensionless group, Bo^2We_D, versus outlet quality, $x_{e,out}$, for (a) single- and (b) double-sided heating, and Bo^2We_D versus inlet quality, $x_{e,in}$, for (c) single- and (d) double-sided heating. In each plot, for the entire range of inlet pressure, p_{in}, the datapoints are segregated by mass velocity in the range of G = 250 – 2000 kg/m^{2}s.

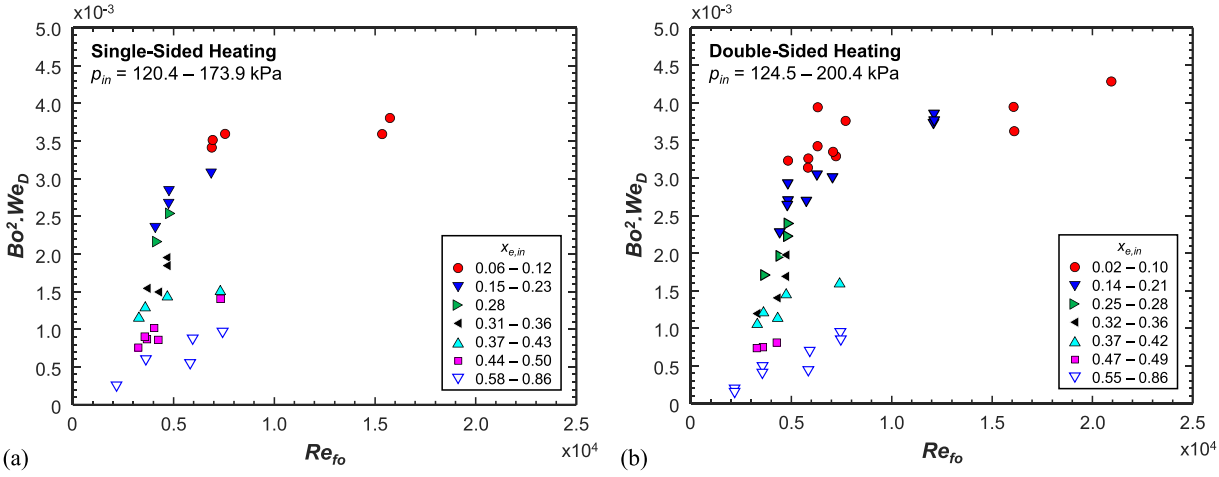

Fig. 17. Variations of dimensionless group, Bo^2We_D,versus liquid-only Reynolds number, Re_{fo}, for (a) single- and (b) double-sided heating. In each plot, the datapoints are segregated into several bands of inlet quality, $x_{e,in}$, for the entire range of inlet pressure, p_{in}.

The next sub-model is based on classical instability theory of two fluids moving at different velocities [49,50]. The stability of the interface between the liquid layer and vapor layer along the heated wall is determined by the relative magnitudes of inertia, surface tension, and body force. Assuming the interface can be modeled as an ideal sinusoid, its critical wavelength, which corresponds to the onset of instability, and interfacial curvature can be determined. An energy balance at the wetting front determines the heat flux required to produce vapor with sufficient momentum to overcome the pressure force associated with the interfacial curvature. A final energy balance equates the heat flux

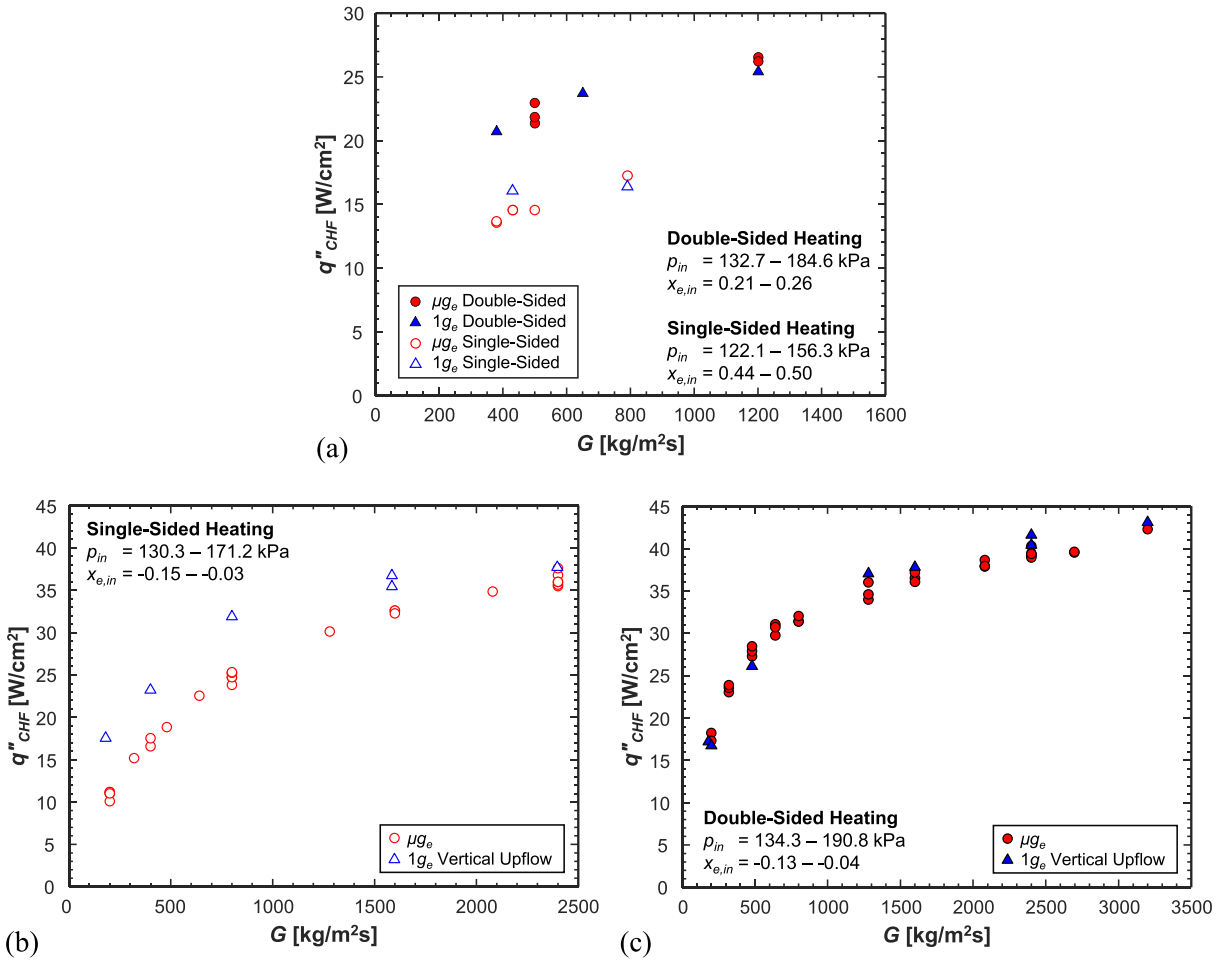

Fig. 18. Comparison of experimental CHF, q''_{CHF}, in microgravity, μg_e, to Earth-gravity, $1g_e$, vertical upflow [30] for (a) two-phase inlet, and subcooled inlet [34] with (b) single- and (c) double-sided heating.

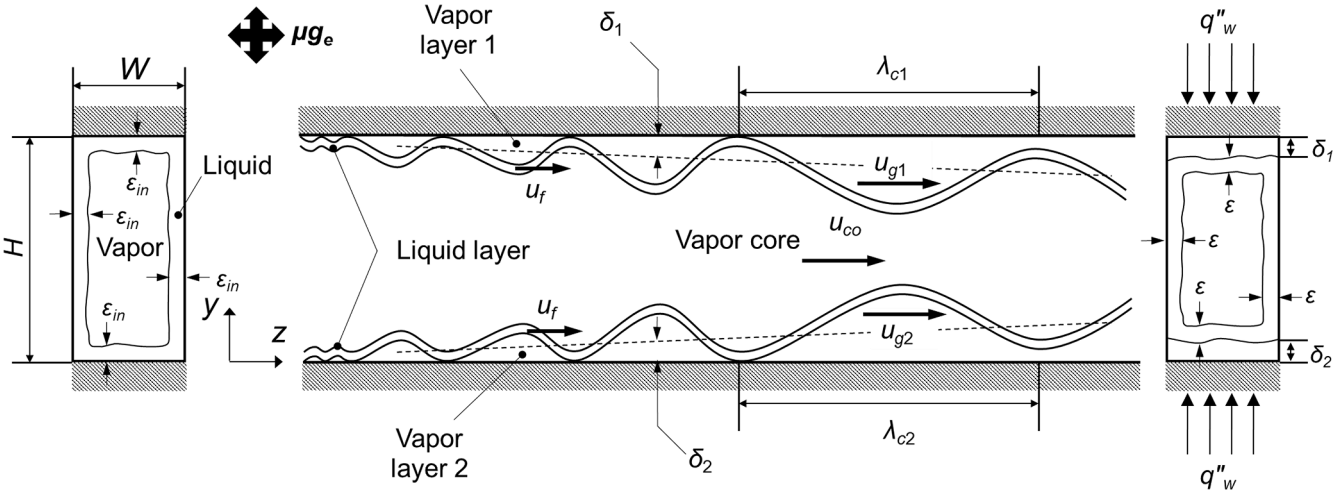

Fig. 19. Schematics of the idealized formation of wavy liquid-vapor interface for double-sided heating in microgravity. A sectional cut along the channel length is shown in the middle, while cross-sections at the inlet and outlet are respectively shown on the left and right sides.

concentrated in the wetting fronts to the entire wall heat.

The model commences with determining the void fraction of the annular core at the inlet by solving the conservation of momentum equations with adiabatic boundary conditions. Then a value of q''_{CHF} is assumed, and the separated flow model is solved via a fourth order Runge-Kutta numerical scheme to determine local flow characteristics along the channel. The separated flow model is solved up to z_o, which corresponds to the axial location where the velocity of vapor along the wall surpasses that of the liquid film. z_o onwards, a critical wavelength, λ_c, is assumed and the axial location z^* is defined as $z^* = z_o + \lambda_c$. The separated flow model is resumed to determine local properties at z^*, at which point a new λ_c is determined as

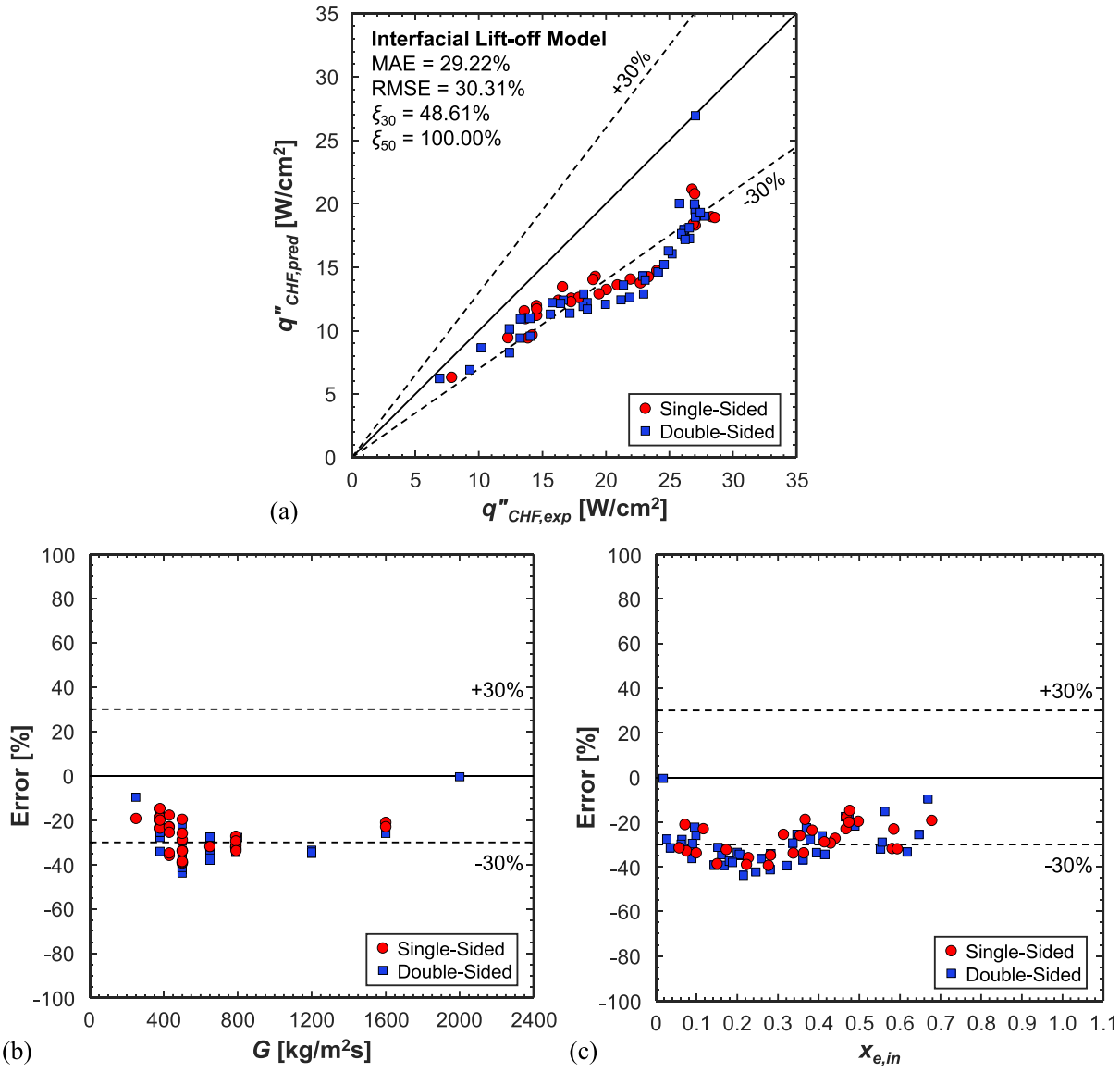

Fig. 20. (a) Parity plot of predictions by the *Interfacial Lift-off Model*, and error of model predictions over the entire range of (b) mass velocity, G, and (c) inlet quality, $x_{e,in}$, for both single- and double-sided heating configurations.

Table 2
Sub-model outputs from the *Interfacial Lift-off Model*.

Heating Configuration	Expt. Case Reference #	G [kg/m²s]	p_{in} [kPa]	T_{in} [°C]	$x_{e,in}$	$q''_{CHF,exp}$ [W/cm²]	$q''_{CHF,pred}$ [W/cm²]	z_o [mm]	λ_c [mm]	δ [mm]	$x_{e,out}$
Single-sided	2154	**429.9**	120.4	66.8	0.59	12.3	9.4	2.35	0.94	0.04	0.65
	2158	**430.3**	124.4	67.0	0.47	14.6	12.0	2.49	1.20	0.06	0.55
	2149	**430.3**	128.7	67.0	0.31	19.2	14.3	2.72	1.78	0.11	0.41
	271	499.9	162.4	73.0	**0.15**	24.0	14.7	4.34	3.41	0.26	0.24
	2155	790.3	129.4	68.5	**0.17**	27.0	18.3	3.08	1.87	0.14	0.24
Double-sided	2110	**379.9**	155.0	72.9	0.65	9.3	6.9	3.72	1.18	0.04	0.75
	2102	**379.9**	156.0	72.9	0.56	10.2	8.7	3.70	1.35	0.05	0.70
	2091	**380.0**	157.7	72.9	0.47	12.4	10.1	3.81	1.63	0.07	0.63
	3050	**379.9**	129.7	67.0	0.37	15.8	12.2	2.89	1.76	0.09	0.55
	2051	499.9	135.2	67.9	**0.18**	22.9	14.3	3.56	2.76	0.18	0.34
	2093	650.4	166.4	74.9	**0.19**	24.6	15.2	4.49	2.49	0.16	0.32
	3054	1199.9	183.3	80.4	**0.20**	26.2	17.4	4.95	1.71	0.10	0.29

Table 3
Select correlations applicable to saturated CHF.

Correlation	Remarks	Recommended/ Validated Applicability Ranges	Assessment Statistics
Darges *et al.* (2022) [51] $Bo = 0.353We_{D_e}^{-0.314}\left(\frac{L_h}{D_e}\right)^{-0.226}\left(\frac{\rho_f}{\rho_g}\right)^{-0.481}\left(1-\left(\frac{\rho_f}{\rho_g}\right)^{-0.094}x_{e,in}\right)$ $\ldots\left(1+0.034\frac{1}{Fr_{\theta,D_e}}\right)\left(1+0.008\frac{Bd_{\theta,D_e}}{We_{D_e}^{0.543}}\right)$ (20)	• Based on inlet conditions • Fluid(s): nPFH • Any orientation • g_e and μg_e • Rectangular channel heated on 1 or 2 opposite walls • Developed from a consolidated database of 417 datapoints	$We_{De} = 15.24 – 19540.26$ $L_h/D_e = 5.73 – 11.46$ $\rho_f/\rho_g = 48.15 – 123.90$ $x_{e,in} = -0.50 – 0.68$ $1/Fr_{\theta,De} = -5.82 – 14.68$ $Bd_{\theta,De} = -864.80 – 865.34$ $Bo = 0.0012 – 0.0285$	MAE = 22.4 % RMSE = 24.5 % $\xi_{30} = 76.0\,\%$ $\xi_{50} = 100.0\,\%$
Katto & Ohno (1984) [52] $q''_{CHF} = q''_o\left(1+K\frac{\Delta h_{sub,in}}{h_{fg}}\right)$ (21a) If $\rho_g/\rho_f < 0.15$: $q''_o = \begin{cases} q''_{o2}, & q''_{o2} < q''_{o3} \\ \max(q''_{o3}, q''_{o4}), & q''_{o2} > q''_{o3} \end{cases}$ (21b) $K = \max(K_6, K_7)$ (21c) If $\rho_g/\rho_f > 0.15$: $q''_o = \begin{cases} q''_{o2}, & q''_{o2} < q''_{o13} \\ \max(q''_{o13}, q''_{o5}), & q''_{o2} > q''_{o13} \end{cases}$ (21d) $K = \begin{cases} K_6, & K_6 > K_7 \\ \min(K_7, K_9), & K_6 < K_7 \end{cases}$ (21e) $\frac{q''_{o2}}{Gh_{fg}} = CWe_L^{-0.043}\frac{D}{L_h}$ (21f) $\frac{q''_{o3}}{Gh_{fg}} = 0.10\left(\frac{\rho_g}{\rho_f}\right)^{0.133}We_L^{-\frac{1}{3}}\frac{1}{1+0.0031\frac{L_h}{D}}$ (21g) $\frac{q''_{o4}}{Gh_{fg}} = 0.098\left(\frac{\rho_g}{\rho_f}\right)^{0.133}We_L^{-0.433}\frac{\left(\frac{L_h}{D}\right)^{0.27}}{1+0.0031\frac{L_h}{D}}$ (21h) $\frac{q''_{o5}}{Gh_{fg}} = 0.0384\left(\frac{\rho_g}{\rho_f}\right)^{0.6}We_L^{-0.173}\frac{1}{1+0.28We_L^{-0.233}\frac{L_h}{D}}$ (21i) $\frac{q''_{o13}}{Gh_{fg}} = 0.234\left(\frac{\rho_g}{\rho_f}\right)^{0.513}We_L^{-0.433}\frac{\left(\frac{L_h}{D}\right)^{0.27}}{1+0.0031\frac{L_h}{D}}$ (21j) $C = \begin{cases} 0.25, & L_h/D < 50 \\ 0.25+0.0009\left(\frac{L_h}{D}-50\right), & 50 \le L_h/D \le 150 \\ 0.34, & L_h/D > 150 \end{cases}$ (21k) $K_6 = \left(\frac{1.043}{4CWe_L^{-0.043}}\right)$ (21l) $K_7 = \left(\frac{5\left(0.0124+\frac{D}{L_h}\right)}{6\left(\frac{\rho_g}{\rho_f}\right)^{0.133}We_L^{-\frac{1}{3}}}\right)$ (21m) $K_8 = 0.416\left(\frac{\left(0.0221+\frac{D}{L_h}\right)\left(\frac{D}{L_h}\right)^{0.27}}{\left(\frac{\rho_g}{\rho_f}\right)^{0.133}We_L^{-0.433}}\right)$ (21n) $K_9 = 1.12\left(\frac{1.52We_L^{-0.233}+\frac{D}{L_h}}{\left(\frac{\rho_g}{\rho_f}\right)^{0.6}We_L^{-0.173}}\right)$ (21o)	• Based on inlet conditions • Fluid(s): Water, anhydrous ammonia, benzene, ethanol, helium I, para-hydrogen, monoisopropylbiphenyl, nitrogen, potassium, R-12, R-21, R-22, R-113, R-114, R-115 • Vertical upflow • Uniformly heated circular tubes • Validated for a consolidated database consisting of over 1000 datapoints	$D = 1 – 38.1$ mm $L_h/D = 5 – 940$ $\rho_g/\rho_f = 0.00027 – 0.517$	MAE = 27.7 % RMSE = 31.6 % $\xi_{30} = 53.3\,\%$ $\xi_{50} = 96.0\,\%$
Basu *et al.* (2011) [53] $Bo_{CHF} = 0.3784\left(\frac{\rho_g}{\rho_f}\right)^{0.051}\left(\frac{L_h}{D}\right)^{-1.03}x_{e,out}^{0.8}$ (22)	• Based on outlet conditions • Fluid(s): R-134a, R-123 • Not orientation-specific • Single circular micro-tubes • Developed using a consolidated database of 193 datapoints	$D = 0.286 – 1.6$ mm $G = 300 – 1500$ kg/m^{2}s $\Delta T_{sub,in} = 5 – 40$°C $x_{e,out} = 0.3 – 1.0$	MAE = 48.9 % RMSE = 75.0 % $\xi_{30} = 48.0\,\%$ $\xi_{50} = 74.7\,\%$
Zhang *et al.* (2006) [54] $Bo = 0.0352\left(We_D+0.0119\left(\frac{L_h}{D_h}\right)^{2.31}\left(\frac{\rho_g}{\rho_f}\right)^{0.361}\right)^{-0.295}$ $\times\left(\frac{L_h}{D_h}\right)^{-0.311}\left(2.05\left(\frac{\rho_g}{\rho_f}\right)^{0.170}-x_{e,in}\right)$ (23)	• Based on inlet conditions • Fluid(s): Water • Not orientation-specific • Uniformly heated small-diameter circular tubes • Developed from a consolidated database containing 3837 datapoints, of which 2539 are saturated and the rest subcooled	$D = 0.33 – 6.22$ mm $L/D = 1.0 – 975$ $p_{out} = 0.101 – 19.0$ MPa $G = 5.33 – 134000$ $x_{e,in} = -2.35 – 0.00$ $x_{e,out} = -1.75 – 0.999$ $q''_{CHF} = 0.00935 – 276$ MW/m^2	MAE = 54.9 % RMSE = 55.7 % $\xi_{30} = 4.0\,\%$ $\xi_{50} = 18.7\,\%$

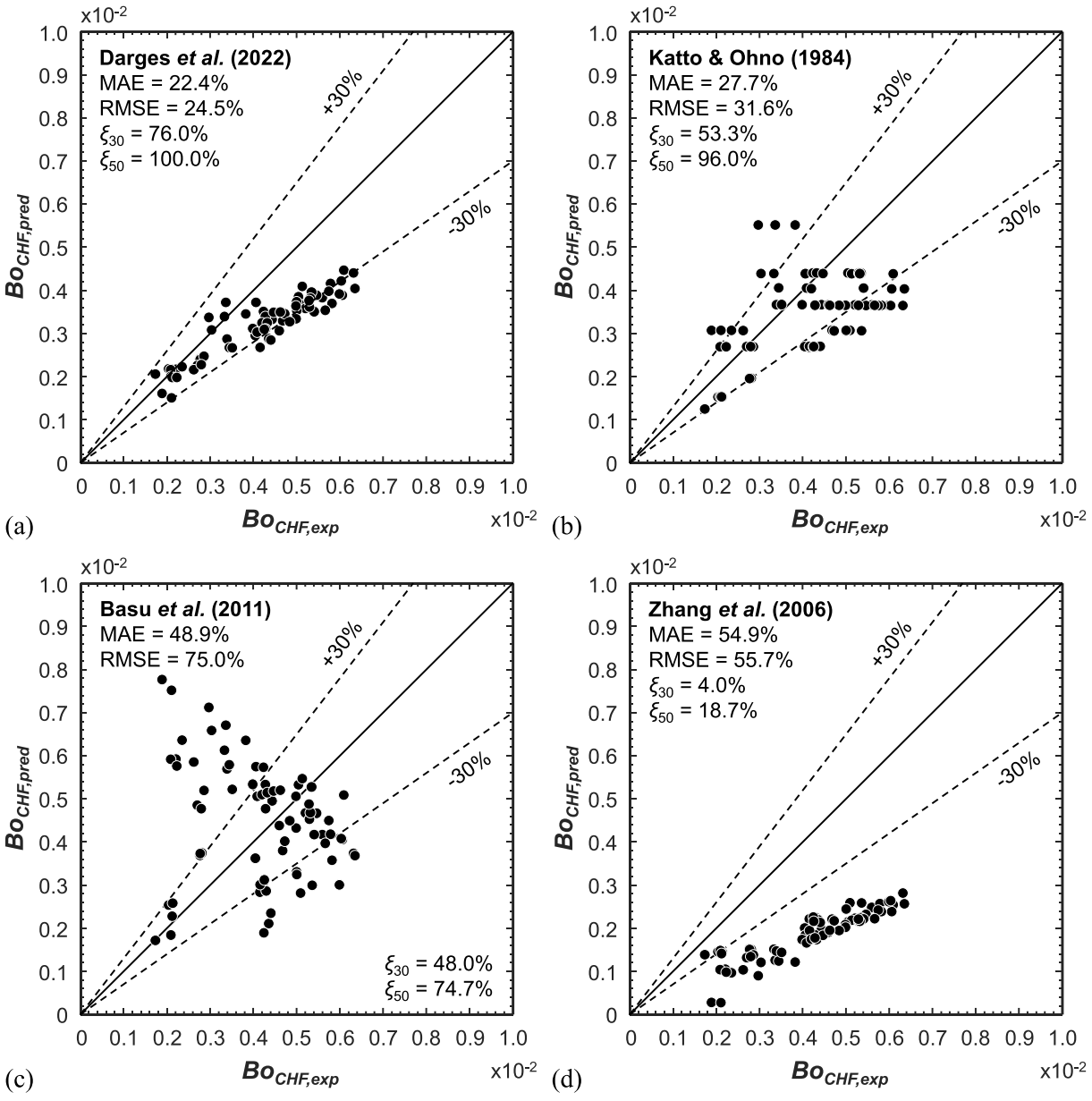

Fig. 21. Parity plots of correlations for saturated CHF: (a) Darges *et al.* (2022) [51], (b) Katto & Ohno (1984) [52], (c) Basu *et al.* (2011) [53] and (d) Zhang *et al.* (2006) [54]. The predictive capability of each correlation is assessed by a combination of mean absolute error (MAE), root mean square error (RMSE), and statistical inliers within ±30 % and ±50 % of experimental CHF value (ξ_{30} and ξ_{50}, respectively).

$$k_{c,a} = \frac{2\pi}{\lambda_{c,a}} = \frac{\rho''_f \rho''_{ga}\left(u_{ga}-u_f\right)^2}{2\sigma\left(\rho''_f+\rho''_{ga}\right)} + \sqrt{\left[\frac{\rho''_f \rho''_{ga}\left(u_{ga}-u_f\right)^2}{2\sigma\left(\rho''_f+\rho''_{ga}\right)}\right]^2 + \frac{\left(\rho_f-\rho_{ga}\right)g_{na}}{\sigma}}, \tag{14}$$

where the modified vapor and liquid densities are defined, respectively, as,

$$\rho''_{ga} = \rho_{ga}\coth(k\delta_a) \tag{15}$$

and

$$\rho''_f = \rho_f \coth\left(k_{c,a}\varepsilon\right). \tag{16}$$

λ_c is iteratively solved for until the assumed and calculated wavelengths are equal. Once λ_c is determined for the assumed heat flux, q''_{CHF} is calculated at z^* as

$$q''_{CHF,a} = \rho_g h_{fg}\left(1-x_{e,in}\right)\left[\frac{4\pi\sigma b}{\rho_g}\sin(\pi b)\right]^{\frac{1}{2}}\frac{\delta_a^{1/2}}{\lambda_{c,a}}\Bigg|_{z^*}. \tag{17}$$

The entire process is iterated until the assumed and calculated q''_{CHF} converge. Typically, for double-sided heating, the procedure is completed for each heated wall separately, and the minimum value obtained defines the true q''_{CHF}. However, in microgravity, the absence of body force results in the λ_c and q''_{CHF} to be identical for both walls.

5.1.2. Comparison of model predictions to experimental data

At high inlet qualities, evidence of any wavy vapor layer is non-existent, so the *Interfacial Lift-off Model* predictions were limited to $x_{e,in} < 0.70$. Outside of this range, the model has not been validated, and errors were exceedingly large. A parity plot of the model's predictions, presented in Fig. 20(a), shows the model generally underpredicts the

current database with an overall MAE of 29.2 %. Both heating configurations were equally well predicted with MAEs of 27.9 % and 30.1 % for single- and double-sided heating, respectively. The errors produced by the model are further investigated in Fig. 20(b) and (c) with respect to G and $x_{e,in}$, respectively. Errors decrease at high G due to experimental q''_{CHF} being constant in this range, whereas the model, generally underpredicting the database, predicts increasing q''_{CHF} with increasing G. Errors are relatively more consistent with respect to $x_{e,in}$ and does not favor either heating configuration.

Outputs from the separated flow model and instability analysis for select cases are presented in Table 2 and highlight the predicted trends of the sub-models. The selected cases, with experimental case reference numbers corresponding to the designation in [35], show trends with respect to G and $x_{e,in}$ for both single- and double-sided heating. The leading columns until $q''_{CHF,exp}$ are inputs into the model, and columns $q''_{CHF,pred}$ and to the right are outputs from various components of the model. Even though the model generally underpredicts $q''_{CHF,exp}$, $q''_{CHF,pred}$ increases with increasing G and decreasing $x_{e,in}$, as observed for $q''_{CHF,exp}$ in Figs. 12 and 13, respectively. For both heating configurations, as $x_{e,in}$ decreases at constant G, the critical wavelength, λ_c, and vapor layer thickness, δ, increase. This can be visually observed by comparing Fig. 7(a) and (d). At lower $x_{e,in}$, greater vapor production results in the interface protruding more distinctly from the heated walls at CHF-. At constant $x_{e,in}$, increasing G results in decreasing λ_c and δ. This is intuitive as higher G increases interfacial shear stress, thinning the vapor layer and is observed comparing Fig. 9(b) and (c). The liquid-vapor interface is more protrusive at lower G at CHF- in Fig. 9(b) than Fig. 9(c). However, comparison of the vapor layers during the extremes of G can be misleading due to the vastly different sizes of HDFs, as shown in Fig. 9(a) and (d).

5.2. Assessment of CHF correlations

The majority of flow boiling CHF correlations available in the literature were developed from data acquired in $1g_e$ and may be unreliable for the present, unique, μg_e database. In a recent study [51], the present authors conducted a comprehensive assessment of flow boiling CHF correlations using a consolidated, pre-launch, FBCE-CHF database. The consolidated database covers broad ranges of operating conditions and different heating configurations, in both $1g_e$, with the channel at different orientations, and μg_e, acquired onboard a parabolic flight. The present database being examined features exclusively two-phase inlet conditions hence, saturated CHF correlations ($x_{e,CHF} \geq 0$) are assessed with the following guidelines:

(i) The length scale prescribed by the original authors is used. Channel diameter, D, is replaced by hydraulic diameter, D_h, in correlations based on D.
(ii) CHF is assumed to occur at the channel's exit such that $L_{CHF} = L_h$ and $x_{e,CHF} = x_{e,out}$.
(iii) Saturated thermophysical properties are evaluated at either the inlet or outlet pressure, as prescribed, using NIST-REFPROP [45].

The best-performing correlations for the subset of the consolidated pre-launch database with two-phase inlet, determined via mean absolute error, MAE, are presently assessed for the ISS database. It is noted that the pre-launch database did not contain any datapoints for two-phase inlet in μg_e, so it is uncertain whether the same conclusions will result from the present assessment. MAE, for N datapoints is determined as

$$MAE(\%) = \frac{1}{N}\sum \left| \frac{q''_{CHF,pred} - q''_{CHF,exp}}{q''_{CHF,exp}} \right| \times 100\%, \quad (18)$$

while root mean square error, RMSE, is defined as

$$RMSE(\%) = \sqrt{\frac{1}{N}\sum \left(\frac{q''_{CHF,pred} - q''_{CHF,exp}}{q''_{CHF,exp}} \right)^2} \times 100. \quad (19)$$

ξ_{30} and ξ_{50} respectively denote the percentage of predictions within ±30 % and ±50 % of $q''_{CHF,exp}$.

Table 3 lists the correlations selected for assessment of the two-phase inlet portion of the ISS database, details concerning their development, and relevant performance statistics, including MAE, RMSE, ξ_{30}, and ξ_{50}. Parity plots of each correlation and the corresponding prediction statistics are shown in Fig. 21. The correlation proposed by the present authors (Darges *et al.* [51]), which was developed with the consolidated pre-launch FBCE database featuring similar inlet conditions near identical test sections, performed the best with a 22.4 % MAE and is shown in Fig. 21(a). This correlation was developed to capture standard trends of flow boiling CHF observed by many other researchers along with the influence of gravity on CHF. Even though the pre-launch database lacked two-phase inlet data in μg_e, the correlation predicted the present database with good accuracy, albeit with a slightly higher MAE than the pre-launch database. Katto and Ohno's correlation [52] performed satisfactorily with a 27.7 % MAE and is featured in Fig. 21(b). Their correlation is widely used for saturated CHF and was validated with a consolidated database containing 15 different fluids and over 1000 datapoints. Even though the database used for development consisted of exclusively vertical upflow data, the correlation predicted the present μg_e database sufficiently well, owing to the minor differences between CHF for two-phase inlet in μg_e and $1g_e$ vertical upflow. Depicted in Fig. 21(c) is the correlation by Basu *et al.* [53], which is the only correlation based on outlet conditions, rather than inlet conditions. Their correlation was developed for a relatively high outlet qualities of $x_{e,out} = 0.3 - 1.0$ and predicts the present database with a 48.9 % MAE. The correlation by Zhang *et al.* [54], presented in Fig. 21(d), was developed from a consolidated CHF database of water in uniformly heated small-diameter tubes with a broad range of operating conditions. Their water-specific correlation underpredicted the present database with a 54.9 % MAE.

In closing, the heat transfer data and flow visualization images presented in this study provide a foundation for CHF modeling, a major pursuit at PU-BTPFL since the 1980s [55,56], as well as ongoing adaptation of machine learning methods, which have shown successes in correlating data for both flow boiling [57-59] and flow condensation [60]. Equally important is the usefulness of both the data and flow visualization results to validation of flow boiling CFD models [61,62].

6. Conclusions

This study investigated critical heat flux (CHF) for microgravity flow boiling of nPFH in a rectangular channel with single- and double-sided heating for two-phase inlet conditions. Experiments were performed as part of the Flow Boiling and Condensation Experiment (FBCE) onboard the International Space Station (ISS), and a sizeable microgravity flow boiling CHF database was amassed. Key conclusions are:

(1) High-speed-video images of flow patterns within FBM's heated length reveal the periodic passing of relatively low-quality, liquid-abundant, High-Density Fronts (HDFs) play a key role in rewetting the wall and facilitating boiling.
(2) The effects of various operating parameters were investigated separately for single- and double-sided heating. For both heating configurations, q''_{CHF} decreases with increasing $x_{e,in}$ in a nearly linear fashion, except at very low $x_{e,in}$. Increasing G enhanced q''_{CHF} with diminishing returns, with q''_{CHF} becoming a constant at high G. The influence of p_{in} and heating configuration on q''_{CHF} was relatively minor. Observed experimental trends are bolstered by non-dimensionalizing the results for easy comparison with other databases.

(3) The new microgravity CHF data was compared with previously acquired CHF data for vertical upflow in Earth gravity. For both heating configurations, the effects of gravity are mitigated by the dominance of flow inertia and interfacial shear stress associated with the inlet void, resulting in similar q''_{CHF}.
(4) Intricate observations of flow patterns revealed features resembling those described by the *Interfacial Lift-off Model*. For $x_{e,in} < 0.70$, the model predicted reasonably well with an overall MAE of 29.2 %, outperforming most empirical correlations.
(5) Select existing correlations were assessed for their predictive capability of the present unique database. A previously proposed correlation by the present authors [51] predicted the data best, evidenced by the least overall MAE of 22.4 %.

CRediT authorship contribution statement

Issam Mudawar: Conceptualization, Funding acquisition, Methodology, Supervision, Writing – review & editing. **Steven J. Darges:** Formal analysis, Software, Validation, Writing – original draft. **V.S. Devahdhanush:** Data curation, Formal analysis, Investigation, Methodology, Writing – original draft, Writing – review & editing.

Declaration of competing interest

The authors declare the following financial interests/personal relationships which may be considered as potential competing interests:
Issam Mudawar reports financial support was provided by NASA.

Data availability

The experimental raw data used in this paper will be publicly made available in a NASA repository.

Acknowledgement

The authors acknowledge the support of the National Aeronautics and Space Administration (NASA) under grant no. 80NSSC22K0328. The authors thank their collaborators at NASA Glenn Research Center, especially Mohammad M. Hasan, Henry K. Nahra, R. Balasubramaniam, and Jeffrey R. Mackey. The authors also thank the FBCE team at NASA Glenn Research Center, Cleveland, Ohio, especially Nancy Hall (FBCE Project Manager), Rochelle May and Phillip Gonia (Software Engineering), Mark Sorrells (Assembly, Integration and Test Lead), Jesse DeFiebre (Fluids Lead), Monica Guzik (FBCE Chief Engineer), and ZIN FCF Mission Operations Team, for their dedicated technical assistance and successful completion of ISS testing of FBCE's FBM.

References

[1] F.P. Chiaramonte, J. McQuillen, H.K. Nahra, P. Manoharan, H. Vanhala, B.J. Motil, J. Kim, V. Carey, W.G. Anderson, J. Plawsky, L. Carter, A. Jackson, 2019 NASA division of space and life and phyiscal sciences research and applications fluid physics workshop report, Cleveland, OH, USA, 2020.
[2] The National Academies, Recapturing a Future for Space Exploration, National Academies Press, Washington, D.C., USA, 2011, https://doi.org/10.17226/13048.
[3] C. Konishi, I. Mudawar, M.M. Hasan, Investigation of localized dryout versus CHF in saturated flow boiling, Int. J. Heat Mass Transfer 67 (2013) 131–146, https://doi.org/10.1016/j.ijheatmasstransfer.2013.07.082.
[4] L.E. O'Neill, I. Park, C.R. Kharangate, V.S. Devahdhanush, V. Ganesan, I. Mudawar, Assessment of body force effects in flow condensation, part II: Criteria for negating influence of gravity, Int. J. Heat Mass Transfer 106 (2017) 313–328, https://doi.org/10.1016/j.ijheatmasstransfer.2016.07.019.
[5] Y. Ma, J.N. Chung, An experimental study of critical heat flux (CHF) in microgravity forced-convection boiling, Int. J. Multiphase Flow 27 (10) (2001) 1753–1767, https://doi.org/10.1016/S0301-9322(01)00031-3.
[6] Y.F. Xue, J.F. Zhao, J.J. Wei, J. Li, D. Guo, S.X. Wan, Experimental study of nucleate pool boiling of FC-72 on smooth surface under microgravity, Microgravity Sci. Tec. 23 (S1) (2011) 75–85, https://doi.org/10.1007/s12217-011-9274-5.
[7] X. Wang, Y. Zhang, B. Qi, J. Zhao, J. Wei, Experimental study of the heater size effect on subcooled pool boiling heat transfer of FC-72 in microgravity, Exp. Therm. Fluid Sci. 76 (2016) 275–286, https://doi.org/10.1016/j.expthermflusci.2016.03.031.
[8] R. Raj, J. Kim, Heater size and gravity based pool boiling regime map: Transition criteria between buoyancy and surface tension dominated boiling, J. Heat Transfer 132 (9) (2010), https://doi.org/10.1115/1.4001635.
[9] B. Liu, B. Yuan, P. Xu, J. Zhao, Y. Zhang, J. Wei, Y. Yang, Q. Cao, A method for approximating the CHF of subcooled flow boiling in microgravity by ground tests, Int. J. Multiphase Flow 122 (2020) 103161, https://doi.org/10.1016/j.ijmultiphaseflow.2019.103161.
[10] H. Ohta, K. Kawasaki, S. Okada, H. Azuma, S. Yoda, T. Nakamura, On the heat transfer mechanisms in microgravity nucleate boiling, Adv. Space Res. 24 (10) (1999) 1325–1330, https://doi.org/10.1016/S0273-1177(99)00741-3.
[11] R.R. Souza, J.C. Passos, E.M. Cardoso, Confined and unconfined nucleate boiling under terrestrial and microgravity conditions, Appl. Therm. Eng. 51 (1–2) (2013) 1290–1296, https://doi.org/10.1016/j.applthermaleng.2012.09.035.
[12] T. Oka, Y. Aba, K. Tanaka, Y.H. Mori, A. Nagashima, Observational study of pool boiling under microgravity, JSME Int. J. Ser. 2 35 (2) (1992) 280–286, https://doi.org/10.1299/jsmeb1988.35.2_280.
[13] M. Saito, N. Yamaoka, K. Miyazaki, M. Kinoshita, Y. Abe, Boiling two-phase flow under microgravity, Nucl. Eng. Des. 146 (1–3) (1994) 451–461, https://doi.org/10.1016/0029-5493(94)90350-6.
[14] M. Narcy, E. de Malmazet, C. Colin, Flow boiling in tube under normal gravity and microgravity conditions, Int. J. Multiphase Flow 60 (2014) 50–63, https://doi.org/10.1016/j.ijmultiphaseflow.2013.11.011.
[15] D.M. Iceri, G. Zummo, L. Saraceno, G. Ribatski, Convective boiling heat transfer under microgravity and hypergravity conditions, Int. J. Heat Mass Transfer 153 (2020) 119614, https://doi.org/10.1016/j.ijheatmasstransfer.2020.119614.
[16] C. Konishi, I. Mudawar, Review of flow boiling and critical heat flux in microgravity, Int. J. Heat Mass Transfer 80 (2015) 469–493, https://doi.org/10.1016/j.ijheatmasstransfer.2014.09.017.
[17] P. Di Marco, W. Grassi, Pool boiling in microgravity: Assessed results and open issues, in: Proc. 3rd European Therm. Conf, Heidelberg, Germany, 2000, pp. 81–90.
[18] R. Raj, J. Kim, J. McQuillen, Pool boiling heat transfer on the International Space Station: Experimental results and model verification, J. Heat Transfer 134 (10) (2012) 101504, https://doi.org/10.1115/1.4006846.
[19] H.S. Lee, H. Merte, F. Chiaramonte, Pool boiling curve in microgravity, J. Thermophys. Heat. Trans. 11 (2) (1997) 216–222, https://doi.org/10.2514/2.6225.
[20] J.F. Zhao, G. Liu, S.X. Wan, N. Yan, Bubble dynamics in nucleate pool boiling on thin wires in microgravity, Microgravity Sci. Tec. 20 (2) (2008) 81–89, https://doi.org/10.1007/s12217-008-9010-y.
[21] J.F. Zhao, J. Li, N. Yan, S.F. Wang, Bubble behavior and heat transfer in quasi-steady pool boiling in microgravity, Microgravity Sci. Tec. 21 (S1) (2009) 175–183, https://doi.org/10.1007/s12217-009-9151-7.
[22] N.J. Penley, C.P. Schafer, J.D.F. Bartoe, The international space station as a microgravity research platform, Acta Astronaut. 50 (11) (2002) 691–696, https://doi.org/10.1016/S0094-5765(02)00003-6.
[23] R. Raj, J. Kim, J. McQuillen, On the scaling of pool boiling heat flux with gravity and heater size, J. Heat Transfer 134 (1) (2012) 011502, https://doi.org/10.1115/1.4004370.
[24] V.K. Dhir, G.R. Warrier, E. Aktinol, D. Chao, J. Eggers, W. Sheredy, W. Booth, Nucleate pool boiling experiments (NPBX) on the International Space Station, Microgravity Sci. Tec. 24 (5) (2012) 307–325, https://doi.org/10.1007/s12217-012-9315-8.
[25] G.R. Warrier, V.K. Dhir, D.F. Chao, Nucleate pool boiling experiment (NPBX) in microgravity: International Space Station, Int. J. Heat Mass Transfer 83 (2015) 781–798, https://doi.org/10.1016/j.ijheatmasstransfer.2014.12.054.
[26] H. Ohta, H. Asano, O. Kawanami, K. Suzuki, R. Imai, Y. Shinmoto, S. Matsumoto, T. Kurimoto, H. Takaoka, K. Fujii, M. Sakamoto, K. Sawada, H. Kawasaki, A. Okamoto, K. Kogure, T. Oka, K. Usuku, T. Tomobe, M. Takayanagi, Development of boiling and two-phase flow experiments on board ISS (research objectives and concept of experimental setup), Int. J. Microgravity Sci. Appl. 33 (2016) 330102, https://doi.org/10.15011/ijmsa.33.330102.
[27] K. Inoue, H. Ohta, Y. Toyoshima, H. Asano, O. Kawanami, R. Imai, K. Suzuki, Y. Shinmoto, S. Matsumoto, Heat loss analysis of flow boiling experiments onboard international space station with unclear thermal environmental conditions (1st report: subcooled liquid flow conditions at test section inlet), Microgravity Sci. Tec. 33 (2) (2021) 28, https://doi.org/10.1007/s12217-021-09869-5.
[28] K. Inoue, H. Ohta, H. Asano, O. Kawanami, R. Imai, K. Suzuki, Y. Shinmoto, T. Kurimoto, S. Matsumoto, Heat loss analysis of flow boiling experiments onboard international space station with unclear thermal environmental conditions (2nd report: liquid-vapor two-phase flow conditions at test section inlet), Microgravity Sci. Tec. 33 (5) (2021) 57, https://doi.org/10.1007/s12217-021-09902-7.
[29] I. Mudawar, Flow boiling and flow condensation in reduced gravity, Adv. Heat Transfer 49 (2017) 225–306, https://doi.org/10.1016/bs.aiht.2017.06.002.
[30] V.S. Devahdhanush, I. Mudawar, H.K. Nahra, R. Balasubramaniam, M.M. Hasan, J. R. Mackey, Experimental heat transfer results and flow visualization of vertical upflow boiling in Earth gravity with subcooled inlet conditions – In preparation for experiments onboard the International Space Station, Int. J. Heat Mass Transfer 188 (2022) 122603, https://doi.org/10.1016/j.ijheatmasstransfer.2022.122603.
[31] V.S. Devahdhanush, S.J. Darges, I. Mudawar, H.K. Nahra, R. Balasubramaniam, M. M. Hasan, J.R. Mackey, Flow visualization, heat transfer, and critical heat flux of flow boiling in Earth gravity with saturated liquid-vapor mixture inlet conditions – In preparation for experiments onboard the International Space Station, Int. J. Heat

Mass Transfer 192 (2022) 122890, https://doi.org/10.1016/j.ijheatmasstransfer.2022.122890.
[32] I. Mudawar, V.S. Devahdhanush, S.J. Darges, M.M. Hasan, H.K. Nahra, R. Balasubramaniam, J.R. Mackey, Heat transfer and interfacial flow physics of microgravity flow boiling in single-side-heated rectangular channel with subcooled inlet conditions – Experiments onboard the International Space Station, Int. J. Heat Mass Transfer 207 (2023) 123998, https://doi.org/10.1016/j.ijheatmasstransfer.2023.123998.
[33] I. Mudawar, V.S. Devahdhanush, S.J. Darges, M.M. Hasan, H.K. Nahra, R. Balasubramaniam, J.R. Mackey, Effects of heating configuration and operating parameters on heat transfer and interfacial physics of microgravity flow boiling with subcooled inlet conditions – Experiments onboard the International Space Station, Int. J. Heat Mass Transfer 217 (2023) 124732, https://doi.org/10.1016/j.ijheatmasstransfer.2023.124732.
[34] I. Mudawar, S.J. Darges, V.S. Devahdhanush, Parametric experimental trends, interfacial behavior, correlation assessment, and interfacial lift-off model predictions of critical heat flux for microgravity flow boiling with subcooled inlet conditions – Experiments onboard the International Space Station, Int. J. Heat Mass Transfer 213 (2023) 124296, https://doi.org/10.1016/j.ijheatmasstransfer.2023.124296.
[35] I. Mudawar, V.S. Devahdhanush, S.J. Darges, M.M. Hasan, H.K. Nahra, R. Balasubramaniam, J.R. Mackey, Microgravity flow boiling experiments with liquid-vapor mixture inlet onboard the International Space Station, Int. J. Heat Mass Transfer (2024) under review.
[36] H. Kumamaru, Y. Koizumi, K. Tasaka, Critical heat flux for uniformly heated rod bundle under high-pressure, low-flow and mixed inlet conditions, J. Nucl. Sci. Tec. 26 (5) (1989) 544–557, https://doi.org/10.1080/18811248.1989.9734345.
[37] C. Konishi, I. Mudawar, M.M. Hasan, Investigation of the influence of orientation on critical heat flux for flow boiling with two-phase inlet, Int. J. Heat Mass Transfer 61 (2013) 176–190, https://doi.org/10.1016/j.ijheatmasstransfer.2013.01.076.
[38] C.R. Kharangate, L.E. O'Neill, I. Mudawar, Effects of two-phase inlet quality, mass velocity, flow orientation, and heating perimeter on flow boiling in a rectangular channel: Part 2 – CHF experimental results and model, Int. J. Heat Mass Transfer 103 (2016) 1280–1296, https://doi.org/10.1016/j.ijheatmasstransfer.2016.05.059.
[39] C.B. Tibiriçá, L.E. Czelusniak, G. Ribatski, Critical heat flux in a 0.38mm microchannel and actions for suppression of flow boiling instabilities, Exp. Therm. Fluid Sci. 67 (2015) 48–56, https://doi.org/10.1016/j.expthermflusci.2015.02.020.
[40] A.S. Dalkılıç, A. Celen, M. Erdoğan, K. Sakamatapan, K.S. Newaz, S. Wongwises, Effect of saturation temperature and vapor quality on the boiling heat transfer and critical heat flux in a microchannel, Int. Commun. Heat Mass Transfer 117 (2020) 104768, https://doi.org/10.1016/j.icheatmasstransfer.2020.104768.
[41] S. Gong, S. Dong, Y. Mei, B. Zhang, Y. Yuan, Z. Zhang, Separate factors' effects on CHF for flow boiling in an inclined rectangular channel under low mass flux, Appl. Therm. Eng. 207 (2022) 118207, https://doi.org/10.1016/j.applthermaleng.2022.118207.
[42] Z. Luo, X. Fang, C. Li, X. Li, Critical heat flux of saturated flow boiling for R245fa under hypergravity, Appl. Therm. Eng. 219 (2023) 119359, https://doi.org/10.1016/j.applthermaleng.2022.119359.
[43] W.A. Arnold, T.G. Hartman, J. McQuillen, Chemical characterization and thermal stressing studies of perfluorohexane fluids for space-based applications, J. Spacecraft Rockets 44 (1) (2007) 94–102, https://doi.org/10.2514/1.22537.
[44] H. Zhang, I. Mudawar, M.M. Hasan, Flow boiling CHF in microgravity, Int. J. Heat Mass Transfer 48 (15) (2005) 3107–3118, https://doi.org/10.1016/j.ijheatmasstransfer.2005.02.015.
[45] E.W. Lemmon, I.H. Bell, M.L. Huber, M.O. McLinden, NIST Standard, Reference Database 23: Reference Fluid Thermodynamic and Transport Properties-REFPROP, Version 10, NIST, Gaithersburg, MD, USA, 2018.
[46] J.E. Galloway, I. Mudawar, CHF mechanism in flow boiling from a short heated wall—II. Theoretical CHF model, Int. J. Heat Mass Transfer 36 (10) (1993) 2527–2540, https://doi.org/10.1016/S0017-9310(05)80191-7.
[47] S.J. Darges, V.S. Devahdhanush, I. Mudawar, H.K. Nahra, R. Balasubramaniam, M. M. Hasan, J.R. Mackey, Experimental results and interfacial lift-off model predictions of critical heat flux for flow boiling with subcooled inlet conditions – In preparation for experiments onboard the International Space Station, Int. J. Heat Mass Transfer 183 (2022) 122241, https://doi.org/10.1016/j.ijheatmasstransfer.2021.122241.
[48] M.S. Bhatti, R.K. Shah, Turbulent and transition flow convective heat transfer in ducts. Handbook of Single-Phase Convective Heat Transfer, Wiley, New York, NY, USA, 1987.
[49] L.M. Milne-Thompson, Theoretical Hydrodynamics, 4th ed., Collier-Macmillan, New York, NY, USA, 1960.
[50] H. Lamb, Hydrodynamics, 6th ed., Dover Publications, New York, NY, USA, 1945.
[51] S.J. Darges, V.S. Devahdhanush, I. Mudawar, Assessment and development of flow boiling critical heat flux correlations for partially heated rectangular channels in different gravitational environments, Int. J. Heat Mass Transfer 196 (2022) 123291, https://doi.org/10.1016/j.ijheatmasstransfer.2022.123291.
[52] Y. Katto, H. Ohno, An improved version of the generalized correlation of critical heat flux for the forced convective boiling in uniformly heated vertical tubes, Int. J. Heat Mass Transfer 27 (9) (1984) 1641–1648, https://doi.org/10.1016/0017-9310(84)90276-X.
[53] S. Basu, S. Ndao, G.J. Michna, Y. Peles, M.K. Jensen, Flow boiling of R134a in circular microtubes—part II: Study of critical heat flux condition, J. Heat Transfer 133 (5) (2011) 1–9, https://doi.org/10.1115/1.4003160.
[54] W. Zhang, T. Hibiki, K. Mishima, Y. Mi, Correlation of critical heat flux for flow boiling of water in mini-channels, Int. J. Heat Mass Transfer 49 (5–6) (2006) 1058–1072, https://doi.org/10.1016/j.ijheatmasstransfer.2005.09.004.
[55] D.E. Maddox, I. Mudawar, Critical heat flux in subcooled flow boiling of fluorocarbon liquid on a simulated electronic chip in a rectangular channel, Int. J. Heat Mass Transfer 32 (2) (1989) 379–394, https://doi.org/10.1016/0017-9310(89)90184-1.
[56] C.O. Gersey, I. Mudawar, Effects of heater length and orientation on the trigger mechanism for near-saturated flow boiling CHF - II. CHF model, Int. J. Heat Mass Transfer 38 (4) (1995) 643–654, https://doi.org/10.1016/0017-9310(94)00193-Y.
[57] Y. Qiu, D. Garg, L. Zhou, C.R. Kharangate, S. Kim, I. Mudawar, An artificial neural network model to predict mini/micro-channels saturated flow boiling heat transfer coefficient based on universal consolidated data, Int. J. Heat Mass Transfer 149 (2020) 119211, https://doi.org/10.1016/j.ijheatmasstransfer.2019.119211.
[58] Y. Qiu, D. Garg, S. Kim, I. Mudawar, C.R. Kharangate, Machine learning algorithms to predict flow boiling pressure drop in mini/micro-channels based on universal consolidated data, Int. J. Heat Mass Transfer 178 (2021) 121607, https://doi.org/10.1016/j.ijheatmasstransfer.2021.121607.
[59] I. Mudawar, S.J. Darges, V.S. Devahdhanush, Prediction technique for flow boiling heat transfer and critical heat flux in both microgravity and earth gravity via artificial neural networks (ANNs), Int. J. Heat Mass Transfer 220 (2024) 124998, https://doi.org/10.1016/j.ijheatmasstransfer.2023.124998.
[60] L. Zhou, D. Garg, Y. Qiu, C.R. Kharangate, S. Kim, I. Mudawar, Machine learning algorithms to predict flow condensation heat transfer coefficient in mini/micro-channel utilizing universal data, Int. J. Heat Mass Transfer 162 (2020) 120351, https://doi.org/10.1016/j.ijheatmasstransfer.2020.120351.
[61] I. Mudawar, J. Lee, Experimental and computational investigation into hydrodynamic and heat transfer characteristics of subcooled flow boiling on the International Space Station, Int. J. Heat Mass Transfer 207 (2023) 124000, https://doi.org/10.1016/j.ijheatmasstransfer.2023.124000.
[62] I. Mudawar, S. Kim, J. Lee, A coupled level-set and volume-of-fluid (CLSVOF) method for prediction of microgravity flow boiling with low inlet subcooling on the International Space Station, Int. J. Heat Mass Transfer 217 (2023) 124644, https://doi.org/10.1016/j.ijheatmasstransfer.2023.124644.